How Does Sea Surface Temperature Drive the Intertropical Convergence Zone in the Southern Indian Ocean?

HONGHAI ZHANG,[a] RICHARD SEAGER,[a] AND SHANG-PING XIE[b]

[a] *Lamont Doherty Earth Observatory, Columbia University, Palisades, New York*
[b] *Scripps Institute of Oceanography, University of California, San Diego, San Diego, California*

(Manuscript received 3 November 2021, in final form 14 April 2022)

ABSTRACT: The Indian Ocean has an intriguing intertropical convergence zone (ITCZ) south of the equator year-round, which remains largely unexplored. Here we investigate this Indian Ocean ITCZ and the mechanisms for its origin. With a weak semiannual cycle, this ITCZ peaks in January–February with the strongest rainfall and southernmost location and a northeast–southwest orientation from the Maritime Continent to Madagascar, reaches a minimum around May with a zonal orientation, grows until its secondary maximum around September with a northwest–southeast orientation, weakens slightly until December, and then regains its mature phase in January. During austral summer, the Indian Ocean ITCZ exists over maximum surface moist static energy (MSE), consistent with convective quasi-equilibrium theory. This relationship breaks up during boreal summer when the surface MSE maximizes in the northern monsoon region. The position and orientation of the Indian Ocean ITCZ can be simulated well in both a linear dynamical model and the state-of-the-art Community Atmosphere Model version 6 (CAM6) when driven by observed sea surface temperature (SST). To quantify the contributions of the planetary boundary layer (PBL) and free-atmosphere processes to this ITCZ, we homogenize the free-atmosphere diabatic heating over the Indian Ocean in CAM6. In response, the ITCZ weakens significantly, owing to a weakened circulation and deep convection. Therefore, in CAM6, the SST drives the Indian Ocean ITCZ directly through PBL processes and indirectly via free-atmosphere diabatic heating. Their contributions are comparable during most seasons, except during the austral summer when the free-atmosphere diabatic heating dominates the mature-phase ITCZ.

SIGNIFICANCE STATEMENT: The intertropical convergence zone (ITCZ) is the globe-encircling band where trade winds converge and strong rainfall occurs in the tropics. Its rains provide life-supporting water to billions of people. Its associated latent heating invigorates the tropical atmospheric circulation and influences climate and weather across the planet. The ITCZ is located north of the equator in most tropical oceans, except in the Indian Ocean where it sits south of the equator year-around. In contrast to the well-known northern ITCZs, the origin of the southern ITCZ in the Indian Ocean remains unknown. This work provides the first explanation for how ocean surface temperature works together with processes in the lower and upper atmosphere to shape the unique ITCZ in the Indian Ocean.

KEYWORDS: Indian Ocean; Intertropical convergence zone; Dynamics; Hadley circulation; Atmosphere-ocean interaction; Sea surface temperature; Diabatic heating

1. Introduction

The intertropical convergence zone (ITCZ) is the globe-encircling band of converging trade winds and maximum rainfall in the tropics (e.g., Schneider et al. 2014). The ITCZ controls the hydrological cycle in the tropics, is intrinsic to tropical climate variability such as El Niño–Southern Oscillation (ENSO) (e.g., Timmermann et al. 2018; Xie et al. 2018) and meridional modes (Chiang and Vimont 2004; Chang et al. 2006; Zhang et al. 2013, 2014, 2015), and regulates climate interactions between the tropics and extratropics (e.g., Cabré et al. 2017; Kang et al. 2018). The ITCZ exhibits significant asymmetry between hemispheres with its zonal and annual mean location around 6°N. This asymmetry is not zonally uniform and the actual ITCZ location ranges from about 10°N in the eastern Pacific to about 4°S in the eastern Indian Ocean. These interhemispheric asymmetries of the ITCZ are still poorly simulated in state-of-the-art climate models, with notorious biases (such as the Pacific double ITCZ) severely hindering models' ability to simulate climate variability and project future climate change (e.g., Lin 2007; Li and Xie 2014; Song and Zhang 2016; Zhou and Xie 2017; Levine and Boos 2017; Xiang et al. 2017; Adam et al. 2018; Seager et al. 2019). Solving these model biases requires a comprehensive understanding of what controls ITCZ asymmetries. Many studies on ITCZ asymmetries have focused exclusively on the zonal mean (Broccoli et al. 2006; Kang et al. 2008; Kang and Held 2012; Donohoe et al. 2012; Kang and Xie 2014; Frierson et al. 2013; Marshall et al. 2014) and others have focused on the same-sign[1] asymmetries in the Pacific and Atlantic where the ITCZ is north of the equator (Mitchell and Wallace 1992, Philander et al. 1996; Xie 1996, 2004; Takahashi and Battisti 2007; Boos and Korty 2016). In contrast, the opposite-sign ITCZ asymmetry in the Indian Ocean remains largely unexplored, except for an earlier work (Zhang 2001) that pointed

Corresponding author: Honghai Zhang, hhzhang@ldeo.columbia.edu; clarkzhang2009@gmail.com

[1] The same-sign or opposite-sign asymmetries are relative to the zonal mean asymmetry.

DOI: 10.1175/JCLI-D-21-0870.1

© 2022 American Meteorological Society. For information regarding reuse of this content and general copyright information, consult the AMS Copyright Policy (www.ametsoc.org/PUBSReuseLicenses).

Unauthenticated | Downloaded 12/07/22 10:48 PM UTC

out the Indian Ocean ITCZ in the context of double ITCZs in observations, a recent paper (Keshtgar et al. 2020) that described the seasonal and interannual variations of the Indian Ocean ITCZ in the ERA-Interim, and a few others (e.g., Neelin and Held 1987; Back and Bretherton 2009a,b) that simply included the Indian Ocean in their general analysis of tropical ITCZs but did not address the Indian Ocean. Here we attempt to investigate the mechanisms underlying the intriguing Indian Ocean ITCZ.

Mechanisms for ITCZ asymmetries have been proposed for the zonal mean and the same-sign asymmetries in the Pacific and Atlantic. For the zonal mean, the location of the ITCZ has been shown to be constrained by the global atmospheric energy balance via the Hadley circulation (Broccoli et al. 2006; Kang et al. 2008). The Hadley circulation transports moisture from the subtropics to the tropics via its lower branch, giving rise to the ITCZ, and transports energy in the opposite direction via its upper branch. The global atmospheric energy balance requires that if the atmosphere in one hemisphere receives net heat (through top and/or bottom boundaries), the atmosphere in the other hemisphere has to release the same amount of heat, which is accomplished by a cross-equatorial atmospheric energy transport to the hemisphere losing heat. This leads to a Hadley circulation cell straddling the equator with rising motion in the heated hemisphere and descending motion in the cooling hemisphere, thus displacing the ITCZ toward the hemisphere receiving heat. In the present climate, it is argued that the oceanic Atlantic meridional overturning circulation moves heat north across the equator and heats the Northern Hemisphere atmosphere, which places the zonal mean ITCZ in the Northern Hemisphere (e.g., Frierson et al. 2013).

In addition to this global energy constraint theory, two local processes involving asymmetries in geography and orography had earlier been proposed to explain the ITCZ asymmetries in the Pacific and Atlantic. On one hand, Philander et al. (1996) argued that the ITCZ asymmetry in these oceans arises from the asymmetric geometries of the west coasts of the tropical Americas and Africa (Xie 1996). The orientation of the western coastline of the Americas relative to meridians, together with the bulge of western Africa to the north of the Gulf of Guinea, generates stronger surface cooling through Ekman-driven coastal upwelling to the south of the equator than to the north, creating a north–south sea surface temperature (SST) asymmetry that favors an ITCZ north of the equator in the eastern Pacific and Atlantic. On the other hand, Takahashi and Battisti (2007) argued that the ITCZ asymmetry in the eastern Pacific is attributable to the orographic forcing from the Andes. Through their mechanical effects on the zonal mean flow, the Andes force dry air to subside into the near-surface boundary layer off the west coast of South America, equatorward of the westerlies (Rodwell and Hoskins 2001). This enhances evaporation, cooling the southeast Pacific and creating the north–south SST asymmetry that favors an ITCZ north of the equator in the eastern Pacific. Similarly, the orographic forcing of the southern African highlands has recently been shown to contribute to the ITCZ asymmetry in the Atlantic (Potter et al. 2017).

These global or local mechanisms are obviously not applicable to the opposite-sign ITCZ asymmetry in the Indian Ocean. In particular, the global energy constraint theory supports a northern ITCZ (Frierson et al. 2013; Marshall et al. 2014) and hence the southern Indian Ocean ITCZ must arise from more local processes. Explaining ITCZ asymmetries often involves an explanation of the underlying SST distribution (e.g., Xie and Philander 1994; Philander et al. 1996; Takahashi and Battisti 2007). However, as a first step, here we take the observed SST distribution as given and attempt to explain how it drives the southern ITCZ in the Indian Ocean. The associated SST distribution will be explained in a future study.

In the next section, we examine various observational and reanalysis datasets to illustrate the climatological features of the Indian Ocean ITCZ and attempt to explain it using known theories. Then we turn to numerical models driven by observed SST to investigate the atmospheric processes underlying the ITCZ. Specifically, we quantify the relative contributions of planetary boundary layer (PBL) and free-atmosphere processes to the Indian Ocean ITCZ, which is a question that has been addressed mostly in terms of the Pacific and Atlantic ITCZs but still remains open [see an excellent review by Sobel (2007) and the references therein]. A summary and discussion conclude this work.

2. Observational analysis

In this work, we define the ITCZ based on combined thresholds of precipitation larger than 4 mm day^{-1} and surface convergence stronger than 2×10^{-6} s^{-1} (i.e., $\nabla \cdot \mathbf{u} \le -2 \times 10^{-6}$ s^{-1}). This intuitive definition is intended to capture the ITCZ as a zone of strong precipitation and surface convergence, as opposed to a line of peak precipitation and/or zero-crossing mass or energy fluxes (e.g., Hwang and Frierson 2013; Adam et al. 2016; Popp and Lutsko 2017; Byrne et al. 2018). The choice of these thresholds is somewhat arbitrary but is not critical for our conclusions. Next, we show that the ITCZ in the southern Indian Ocean is a robust climatological feature year-round across various datasets, including ship-based and satellite observations. In particular during boreal summer, the southern ITCZ occurs in addition to the precipitation maximum north of the equator associated with the South Asian summer monsoon (SASM). Although the SASM is often interpreted as the seasonal migration of the main ITCZ in the Indian Ocean (e.g., Nie et al. 2010; Gadgil 2018; Keshtgar et al. 2020), monsoons differ from ITCZs in many aspects such as their dynamical balance [see recent reviews by Biasutti et al. (2018) and Geen et al. (2020), and references therein]. For this reason, we hereafter retain the term "monsoon" and use it to refer to the SASM (even though the SASM satisfies our ITCZ definition). The year-round ITCZ in the southern Indian Ocean is the focus of this work.

Figures 1 and 2a show the climatological (1981–2010) seasonal cycle of precipitation from the CPC Merged Analysis of Precipitation (CMAP) standard product, a blend of satellite and gauge data (Xie and Arkin 1997), and 1000-hPa winds and associated divergence from the latest ERA5 dataset (Hersbach et al. 2020), both at 1° resolution [very similar results are also obtained from the Global Precipitation Climatology

Unauthenticated | Downloaded 12/07/22 10:48 PM UTC

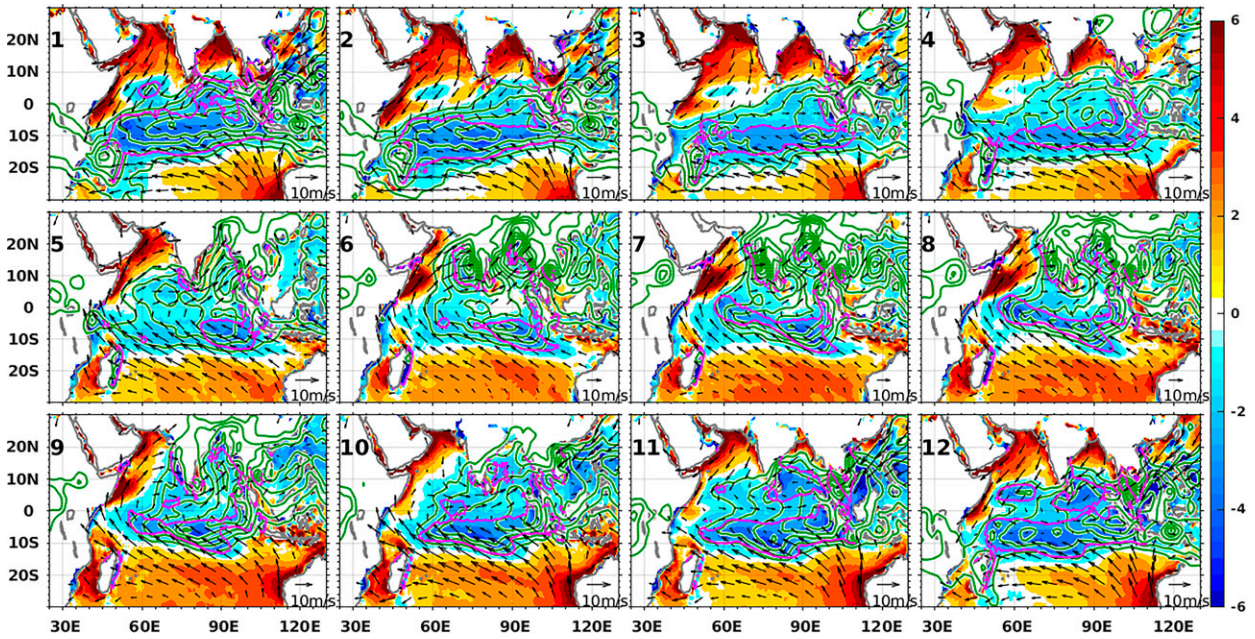

FIG. 1. Monthly climatology (1981–2010) of precipitation (mm day^{-1}; green contours) from the CMAP standard product, 1000-hPa winds (m s^{-1}; vectors), and divergence (10^{-6} s^{-1}; shading) from the ERA5 dataset. The -2×10^{-6} s^{-1} divergence isoline is highlighted in magenta contours. The precipitation contours start from 4 mm day^{-1} and are plotted every 2 mm day^{-1}. A scale vector of 10 m s^{-1} is shown in the lower-right corner of each panel. The Arabic number in the upper-left corner of each panel indicates the calendar month (1 for January, 2 for February, etc.).

Project (GPCP) and the NCEP–DOE Reanalysis II dataset (not shown)]. Throughout the year, the southern tropical Indian Ocean (about 0°–15°S) exhibits the defining features of an ITCZ, including strong surface wind convergence and precipitation with local maxima. This southern ITCZ migrates with a weak semiannual cycle. It peaks around January to February with strongest rainfall, southernmost location, and basinwide longitudinal span tilted from the

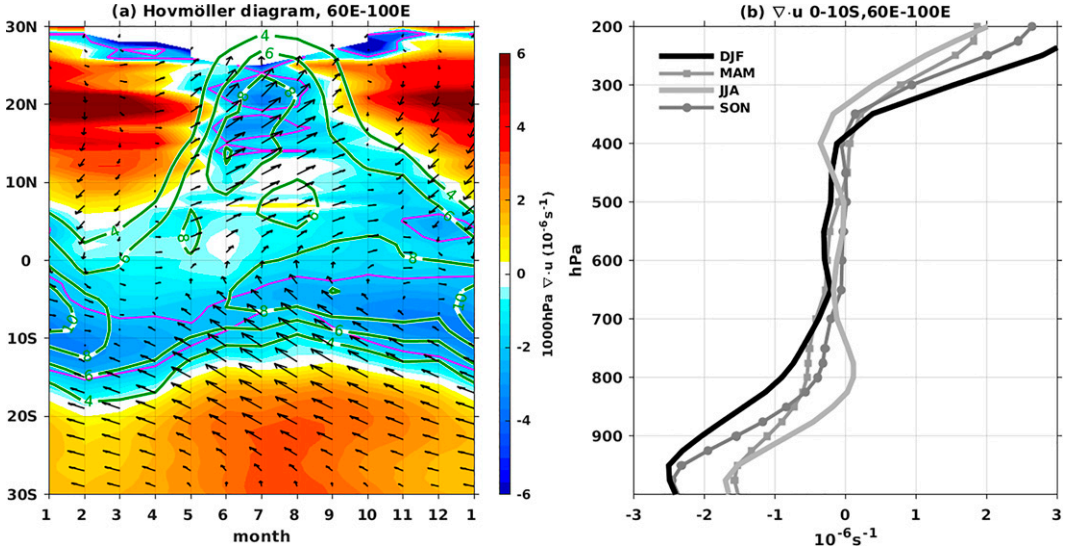

FIG. 2. (a) Climatological seasonal cycle (1981–2010) of the CMAP precipitation (green contours at 4, 6, 8, … mm day^{-1}), the ERA5 1000-hPa winds (m s^{-1}; vectors) and divergence (10^{-6} s^{-1}; shading, with the -2×10^{-6} s^{-1} isoline highlighted in magenta contour) zonally averaged between 60° and 100°E. The wind vectors are plotted as $\langle u/5, v \rangle$ (as opposed to the normal vector $\langle u, v \rangle$), in which the 1/5 factor applied to zonal winds is merely for display purposes. (b) Vertical profile of the horizontal wind divergence averaged over the southern Indian Ocean 0°–10°S, 60°–100°E for DJF in black, MAM in gray with squares, JJA in gray, and SON in gray with dots.

Unauthenticated | Downloaded 12/07/22 10:48 PM UTC

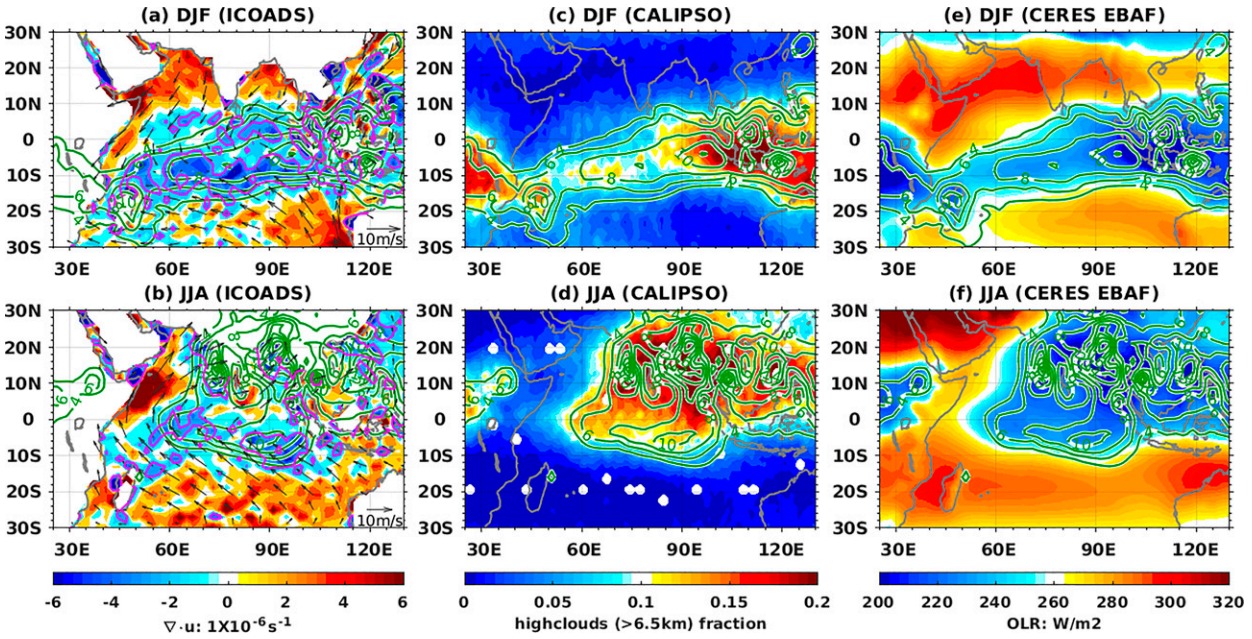

FIG. 3. Seasonal climatology of precipitation from CMAP (green contours at 4, 6, 8, … mm day^{-1}) and (a),(b) ICOADS surface winds (m s^{-1}; vectors) and associated divergence (10^{-6} s^{-1}, shading, with the -2×10^{-6} s^{-1} isoline highlighted in magenta contour) during 1950–79, (c),(d) *CALIPSO* high-cloud (>6.5 km or <440 hPa) fraction (nondimensional) during 2006–20 (colors), and (e),(f) CERES EBAF outgoing longwave radiation (W m^{-2}) during 2005–15 (colors). Rows denote the seasonal average during (top) DJF and (bottom) JJA.

Maritime Continent southwestward to Madagascar (see the magenta contour of -2×10^{-6} s^{-1} divergence and the green contour of 4 mm day^{-1} precipitation). From March to May, it weakens with strong precipitation (>6 mm day^{-1}) retreating to the east of about 70°E and migrates closer to the equator. From May to August, it grows (i.e., intensifies in strength and expands in size) and extends northwestward along with the development of the SASM. The southern ITCZ reaches its second maximum in precipitation (Fig. 2a) around September with a largely zonal orientation, and slightly weakens until December before maturing again in January. Over the southern ITCZ region, the height of horizontal convergence varies seasonally, ranging from about 800 hPa during June–August (JJA) up to about 400 hPa during December–February (DJF) (Fig. 2b). The surface convergence associated with the southern ITCZ appears to result from different processes in different seasons (Fig. 1): in austral summer it is a result of the convergence of southeast and northeast trade winds (i.e., akin to the ITCZs seen in the eastern Pacific and Atlantic), but in austral winter it is a result of the slowdown of the southeast trade winds as they approach the equator. Note that during June–August, the precipitation associated with the southern ITCZ is secondary to the SASM rainfall. All of these characteristics make the ITCZ in the southern Indian Ocean unique and intriguing.

We have also examined other independent observational datasets, including the ship-based marine surface winds from the International Comprehensive Ocean–Atmosphere Dataset (ICOADS) (Freeman et al. 2017) and satellite observations of high cloud fraction from the GCM-Oriented Cloud *CALIPSO* Product (GOCCP) (Winker et al. 2009) and outgoing longwave radiation (OLR) from the Clouds and the Earth's Radiant Energy System (CERES) Energy Balanced and Filled (EBAF) Edition 4.1 (Loeb et al. 2018). To highlight the robustness of the southern ITCZ in the Indian Ocean as a climatological feature, we analyze the ship-based and satellite datasets from different periods than the 1981–2010 period used for CMAP and ERA5: ICOADS winds during 1950–79, *CALIPSO* clouds during 2006–20, and CERES EBAF radiation during 2005–15. Figure 3 shows these fields in the Indian Ocean averaged during DJF and JJA. Despite the nonoverlapping periods analyzed, the ship-based ICOADS surface winds and associated divergence are consistent with those from ERA5 (Fig. 1) during both seasons, with surface convergence beneath strong precipitation in the ITCZ region resulting from the converging northeast and southeast trades during DJF and the slowdown of the southeast trades during JJA (Figs. 3a,b). The ITCZ in the southern Indian Ocean is also collocated with relatively large values in high cloud (>6.5 km) fraction (Figs. 3c,d) and relatively small values in OLR (Figs. 3e,f), consistent with the deep convection often associated with ITCZs. Note that the basinwide maximum in high cloud fraction and the basinwide minimum in OLR are observed over the Maritime Continent during DJF and over the SASM region during JJA, which suggests stronger convection in these regions than in the southern ITCZ region. In particular, during JJA, the strong precipitation over the SASM region (especially the Bay of Bengal) and the associated maximum high cloud fraction and minimum OLR have been interpreted as the ITCZ in the Indian Ocean (e.g., Nie et al. 2010; Gadgil 2018; Keshtgar et al. 2020), while the ITCZ in the southern Indian Ocean has not been considered as a rainy ITCZ

Unauthenticated | Downloaded 12/07/22 10:48 PM UTC

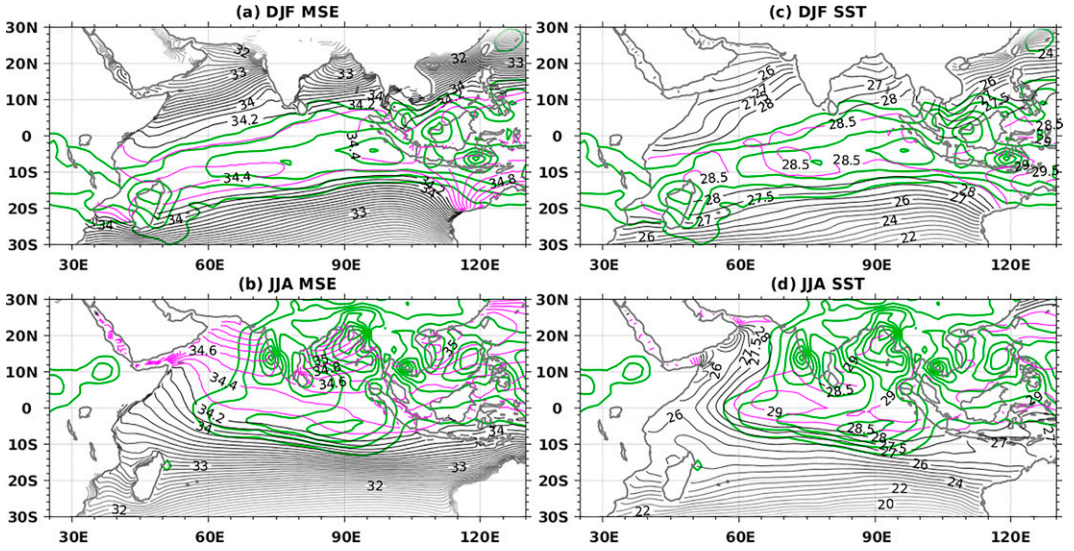

FIG. 4. Seasonal climatology of (a),(b) ERA5 1000-hPa moist static energy (10^4 J kg^{-1}; black and magenta contours) and (c),(d) HadISST SST (°C; black and magenta contours) during 1981–2010. Large MSE (>34.2 × 10^4 J kg^{-1}) and SST (>28°C) are highlighted in magenta contours. Green contours (4, 6, 8, … mm day^{-1}) are the corresponding precipitation climatology from CMAP. Rows denote the seasonal average during (top) DJF and (bottom) JJA.

until the advent of microwave satellite data showing a local precipitation maximum consistent with the ship-based surface convergence (Fig. 3b). Taken together, various independent observations and reanalysis datasets demonstrate that the Indian Ocean has a robust ITCZ to the south of the equator all year round.

What physical processes drive the year-round ITCZ in the southern Indian Ocean? The convective quasi-equilibrium (CQE) theory (e.g., Arakawa and Schubert 1974; Emanuel et al. 1994) predicts that the ITCZs should occur over regions of maximum surface equivalent potential temperature or moist static energy (MSE) (e.g., Privé and Plumb 2007; Geen et al. 2020, and references therein). Here we examine this theory in the Indian Ocean by comparing the seasonal mean precipitation and MSE at 1000 hPa from the ERA dataset (Figs. 4a,b). During DJF, the precipitation associated with the Indian Ocean ITCZ is well collocated with the maxima in surface MSE (Fig. 4a), consistent with CQE theory. During JJA, the surface MSE maximizes in the SASM region and decreases monotonically toward and through the southern ITCZ region, which appears to be inconsistent with CQE theory in that the southern ITCZ is not collocated with an MSE maximum. The horizontal structure of surface MSE can be explained mostly by the distribution of SST during DJF (Fig. 4c), whereas during JJA, as the SST does not increase monotonically from the southern ITCZ region to the SASM region (Fig. 4d), the surface MSE pattern must also have contributions from the moisture distribution (which in turn depends mostly on SST but also atmospheric circulation). Overall, based on observations and CQE theory, the ITCZ in the southern Indian Ocean during DJF appears to be a typical ITCZ that resides over maxima in surface MSE, but during JJA CQE theory fails to explain the ITCZ in the southern Indian Ocean (although it explains the low-level convergence over the SASM region).

Next, we will turn to numerical models to further explore the physical processes underlying the Indian Ocean ITCZ.

3. Modeling results

The main purpose of this section is to understand the atmospheric processes associated with the ITCZ in the southern Indian Ocean, given the observed SST. Two models of distinct degrees of complexity are used, including a simple linear dynamical model and a state-of-the-art atmosphere general circulation model (AGCM) with a complex suite of parameterized physics. The linear model is used to examine the ability of linear dynamics to simulate the ITCZ in the southern Indian Ocean, while the AGCM is used to disentangle the relative roles of the PBL versus free-atmosphere processes in the Indian Ocean ITCZ (a question that the linear model is unable to solve).

a. Linear model simulations

The linear model used here is derived directly from the model of Lindzen and Nigam (1987), which was constructed as a PBL model to examine the role of SST gradients in forcing low-level winds and convergence in the tropics while neglecting the free-atmosphere impacts. In the original model, the zonal mean and eddy components (deviations from the zonal mean) were solved separately with different sets of equations, with the eddy equations including several additional terms that have later been shown to be small and negligible (Neelin 1989). In this work, we neglect those small terms and combine the two components to form a set of equations

Unauthenticated | Downloaded 12/07/22 10:48 PM UTC

for the total field (see appendix for derivation). The governing equations can be written in the following form:

$$\varepsilon u - fv + g\frac{\partial \hbar}{\partial x} = 0,$$

$$\varepsilon v - fu + g\frac{\partial \hbar}{\partial y} = 0,$$

$$\varepsilon_T \hbar + H_0\left(\frac{\partial u}{\partial x} + \frac{\partial v}{\partial y}\right) = -Q,$$

where u and v are the mass-weighted horizontal winds vertically averaged through the depth of the PBL; $\hbar$ is a transformed variable defined as $\hbar \equiv h - (H_0/2T_0)T_s$ with h being the perturbation in the PBL height and T_s being the prescribed surface temperature in the original model (T_0 and H_0 are reference temperature and height, respectively); and $Q = (H_0/2T_0\tau_c)T_s$ is a forcing term linearly related to T_s, where τ_c represents the adjustment time of the PBL height as the cumulus convection responds to boundary layer convergence; finally, ε is the Rayleigh friction coefficient and $\varepsilon_T = 1/\tau_c$ amounts to a thermal damping for $\hbar$.

The form of this set of equations is mathematically identical to that of the more well-known model of Gill (1980). However, these two models have very different physical arguments. As stated above, the Lindzen–Nigam model is a PBL model and assumes that the boundary winds are driven by horizontal pressure gradients resulting from SST gradients (i.e., neglecting contributions from the free atmosphere), while the Gill model is interpreted as a free-atmosphere model and the condensational heating associated with deep convection drives surface winds. The differences and similarities between the Lindzen–Nigam model and the Gill model have been well discussed in the literature (e.g., Wang and Li 1993; Chiang et al. 2001; Sobel 2007). Considering these physical ambiguities, the linear model could be interpreted either as a PBL model as originally intended, or as a free-atmosphere model. Either way, it can illustrate the skill of linear dynamics in simulating the low-level winds and convergence in the Indian Ocean given the SST.

The SST imposed in the linear model is taken from the Met Office Hadley Centre's sea ice and SST dataset (HadISST) version 2 (Titchner and Rayner 2014), and is extrapolated over land by solving Poisson's equation (similar results are obtained without the extrapolation; not shown). As in Lindzen and Nigam (1987), the model is actually driven by virtual surface temperature: $T_{vs} = T_s(1 + w/0.622)/(1 + w)$, where w is the mixing ratio taken from ERA5. All the parameters used here are the same as those in the original Lindzen–Nigam model and we solve the model on an equatorial beta plane with a grid spacing of about 222 km. Figure 5 compares the horizontal divergence field computed from the linear model with the ERA5 low-level horizontal divergence vertically averaged over 1000–700 hPa (corresponding approximately to the PBL depth assumed in the linear model). During DJF and JJA (also spring and fall; not shown), the linear model fairly well reproduces the spatial pattern of the ERA5 low-level wind divergence in the Indian Ocean. In particular, the orientation of the

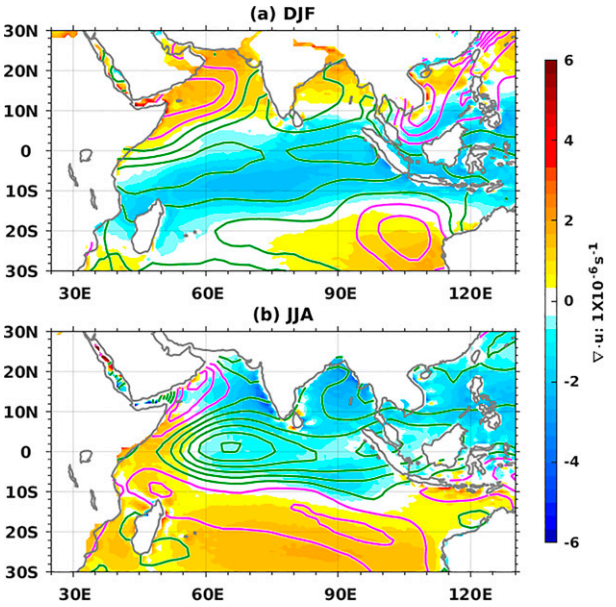

FIG. 5. (a) DJF and (b) JJA climatology of ERA5 horizontal divergence (10^{-6} s^{-1}; shading) vertically averaged over 1000–700 hPa compared with the low-level divergence from the linear model (contours; negative in green and positive in magenta, starting at $\pm 0.2 \times 10^{-6}$ s^{-1} with an interval of $\pm 0.4 \times 10^{-6}$ s^{-1}).

low-level convergence associated with the ITCZ in the southern Indian Ocean is well captured in the linear model. There are also obvious biases. For example, the linear model simulates the strongest convergence farther equatorward than seen in ERA5 (even on the equator during JJA); over the Bay of Bengal, it fails to simulate the divergence in ERA5 during DJF. Most of these successes and biases can be explained intuitively by the thermodynamic equation of the model, which describes a balance among the boundary forcing [$Q = (H_0/2T_0\tau_c)T_s$], low-level wind divergence ($\partial u/\partial x + \partial v/\partial y$), and thermal damping ($\varepsilon_T \hbar$). Since the thermal damping only affects amplitude (not the spatial pattern), the pattern of the low-level divergence (or convergence) should follow the pattern of the forcing, with maximum convergence expected to occur where the forcing is strongest—that is, where the maximum SST is. This is indeed the case in the model to a first-order approximation (cf. the SST in Figs. 4c,d and the divergence in Figs. 5a,b). This model behavior is consistent with observations that most ITCZs reside over warmest SSTs.

Overall, the solution from the linear model shows that, given the observed SST, linear dynamics can realistically capture the spatial pattern, especially the orientation, of the low-level convergence associated with the ITCZ in the southern Indian Ocean. However, how the given SST drives low-level winds via atmospheric processes in this linear model is not clear, which will be addressed in the next section with AGCM experiments.

b. AGCM simulations

We use the Community Atmosphere Model version 6.3 (CAM6) within the Community Earth System Model version

Unauthenticated | Downloaded 12/07/22 10:48 PM UTC

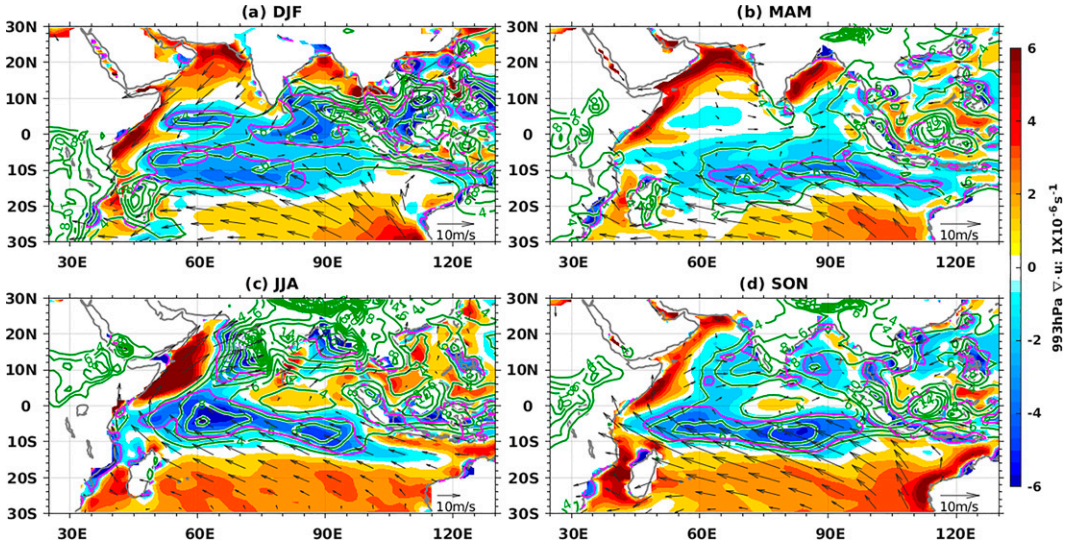

FIG. 6. Seasonal climatology of precipitation (green contours; mm day^{-1}), 993-hPa winds (vectors; m s^{-1}), and divergence (shading; 10^{-6} s^{-1}, with the -2×10^{-6} s^{-1} isoline highlighted in magenta contour) in the CAM6 control simulation: (a) DJF, (b) MAM, (c) JJA, and (d) SON. Precipitation contours start at 4 mm day^{-1} and increase every 2 mm day^{-1}. A 10 m s^{-1} reference vector is shown in the lower-right corner of each panel.

2.1.3 (CESM2) (Danabasoglu et al. 2020) to disentangle the relative contributions of the PBL and free-atmosphere processes to the ITCZ in the southern Indian Ocean. CAM6 is a state-of-the-art AGCM and its dynamics and physics are summarized in Danabasoglu et al. (2020). Most relevant to our purpose, the PBL in CAM6 is represented by a high-order turbulence closure known as Cloud Layer Unified by Binormals (CLUBB), which is a unified parameterization of the PBL and shallow convection achieved through a trivariate probability density function (Golaz et al. 2002; Bogenschutz et al. 2013). The deep convection is represented by the Zhang–McFarlane scheme (Zhang and McFarlane 1995), which is a convective available potential energy (CAPE)-based quasi-equilibrium closure. All CAM6 experiments conducted in this work employ the nominal 1° (1.25° in longitude and 0.9° in latitude) horizontal resolution with preindustrial level atmosphere composition and radiative forcings. The surface boundary conditions are the same repeating climatological annual cycle of SST and sea ice from observations. All experiments are integrated for 6 years and the last 4 years are used in analysis.

The control simulation (CNTL) of CAM6 realistically simulates low-level (993 hPa) winds, associated divergence, and precipitation in the Indian Ocean compared to the CMAP observations and the ERA5 dataset. Specifically, CAM6 well captures the location and orientation of the year-round ITCZ in the southern Indian Ocean (as characterized by the isolines of 4 mm day^{-1} precipitation and -2×10^{-6} s^{-1} divergence) (cf. Fig. 6 and Fig. B1 in appendix B). In this southern ITCZ region, the main biases (Fig. B2 in the appendix B) include too-weak precipitation throughout the year but especially during DJF and too-strong low-level convergence from about June to November. In the SASM region during the monsoon season, CAM6 simulates too-strong precipitation and low-level convergence over land and the eastern Arabian Sea but too-weak precipitation and low-level convergence over the Bay of Bengal and the South China Sea. These biases and the associated causes need further analysis (e.g., Lin 2007). Nonetheless, the overall performance of CAM6 warrants its usage to disentangle the atmospheric processes associated with the ITCZ in the southern Indian Ocean. We will focus on the DJF and JJA seasons, when the features of the ITCZ in the southern Indian Ocean are most different (i.e., in terms of precipitation, surface winds, and associated divergence).

To quantify the relative contributions of the PBL and free troposphere processes to the ITCZ in the southern Indian Ocean, we conduct perturbation experiments that are the same as the CNTL except that we homogenize the diabatic heating in the free atmosphere over the Indian Ocean. The hypothesis is that the imposed SST forcing should drive the ITCZ through both PBL processes (e.g., the Lindzen–Nigam argument) and free-atmosphere processes (e.g., deep convection should affect horizontal pressure gradients in the PBL and therefore surface winds). In nature and CAM6 (Fig. 7a), the free-atmosphere diabatic heating in the tropics exhibits a distinct horizontal structure, with net diabatic warming over the ITCZ regions (balancing the adiabatic cooling from ascent) and net diabatic cooling over the subsidence regions (balancing the adiabatic warming from descent). This structured free-atmosphere diabatic heating has long been considered to contribute to the similarly structured surface divergence field (i.e., convergence below diabatic warming and divergence below diabatic cooling) (e.g., Wu et al. 1999, 2000; Sobel 2007; Tomassini 2020). If we horizontally homogenize the diabatic heating in the free atmosphere, the impacts of its horizontal gradients on the surface will be removed and the remaining structure of the surface divergence can be unambiguously attributed

Unauthenticated | Downloaded 12/07/22 10:48 PM UTC

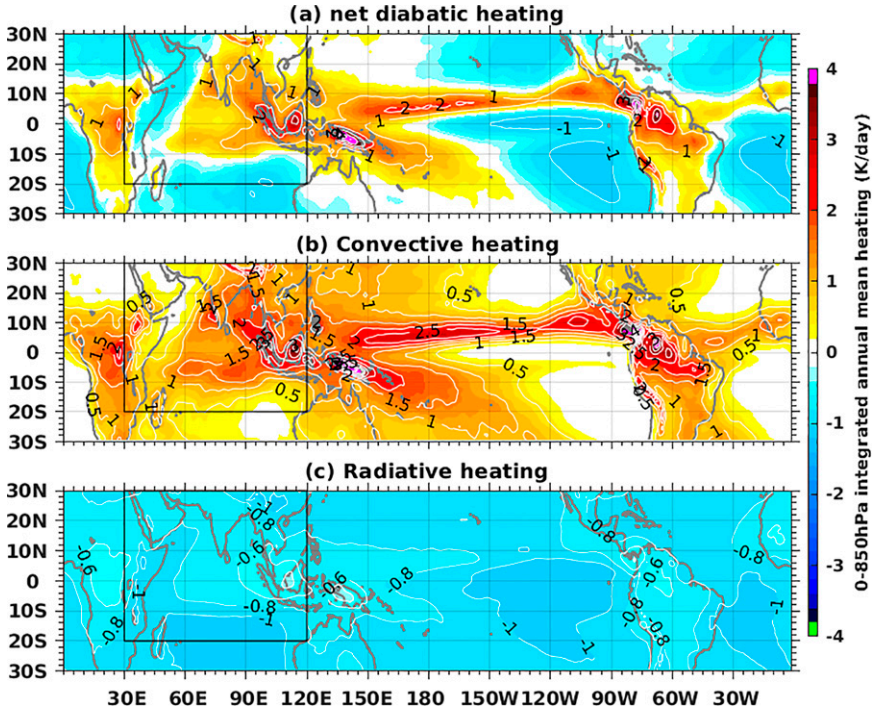

FIG. 7. Annual mean diabatic heating (K day^{-1}) vertically averaged (mass weighted) from 850 hPa to model top in CAM6 control simulation: (a) net diabatic heating (diagnosed heating due to all physical parameterizations), (b) heating associated with convective parameterizations, and (c) heating associated with radiative parameterizations. The contour interval is 1 K day^{-1} in (a), 0.5 K day^{-1} in (b), and 0.2 K day^{-1} in (c). In CAM6, the net diabatic heating is largely composed of convective heating and radiative heating [i.e., the residual, (a) − (b) − (c), is a few orders of magnitude weaker]. The black box denotes the region in the Indian Ocean where the diabatic heating in the atmosphere is homogenized.

to the PBL processes. The contributions of the free-atmosphere structured diabatic heating to the surface divergence can also be quantitatively deduced by comparing the perturbation with control simulations.

To focus on the Indian Ocean ITCZ, we homogenize diabatic heating in the atmosphere above 800 hPa over the Indian Ocean (20°S–30°N, 30°–120°E; i.e., the target region, indicated by the black box in Fig. 7). The choice of the target region is somewhat arbitrary except that it is chosen to cover the southern ITCZ and the northern monsoon regions. Choosing a different target region (30°S–0°, 30°–120°E, or the entire tropics 30°S–30°N) changes results quantitatively, but does not qualitatively change our conclusions (not shown). Over the target region at each model time step, we compute the area-weighted domain average of the diabatic heating calculated by the model on the same pressure levels and then use this domain average value to overwrite the model-calculated heating in the thermodynamic equation. This homogenization is equivalent to reducing the diabatic warming and cooling seen by the thermodynamic equation over the target region and the amplitude of the reduction varies with space and time (depending on the model-calculated heating at each time step). Note that the homogenization conserves the areal mean heating over the target region. A buffer zone (50 hPa vertically and about 6.5° horizontally) is implemented, in which the domain average heating is linearly merged with the model-calculated heating. Outside the target region, horizontal winds and specific humidity throughout the atmosphere are nudged toward the control simulation with a 6-h relaxation time scale. The reason for nudging is to minimize the remote feedbacks that potential changes in the atmosphere outside the target region (in response to the homogenization through wave dynamics) might have on the target region, which allows us to isolate the processes within the Indian Ocean.

We have conducted three homogenization experiments (Table 1). The first experiment is to remove the impacts of horizontal gradients of *total* diabatic heating in the free atmosphere and thus isolate the impacts of the PBL processes on the ITCZ in the southern Indian Ocean (note that the effects of the domain-averaged diabatic heating are still included). In this experiment, we homogenize the diabatic heating associated with all physical parameterizations in CAM6 (termed AllN). The physical parameterizations in CAM6 include three packages: 1) convective processes (penetrative convection, shallow convection, vertical diffusion, and large-scale stable condensation), 2) radiation (with cloud parameterization), and 3) turbulent mixing (gravity wave drag, Rayleigh friction near the model top). The turbulent mixing in CAM6 is negligible

Unauthenticated | Downloaded 12/07/22 10:48 PM UTC

TABLE 1. Summary of CAM6 experiments.

CAM6 expt	Forcing/perturbations
CNTL	Preindustrial-level atmospheric composition and radiation, observed SST, and sea ice annual cycle
AllN	Homogenize all diabatic heating over the Indian Ocean (20°S–30°N, 30°–120°E) above 800 hPa and nudge U, V, and Q back to CNTL outside the homogenization region
ConN	As in AllN, except only homogenizing the heating associated with convection
RadN	As in AllN, except only homogenizing the heating associated with radiation

and the total diabatic heating is dominated by the convective heating from package 1 and the radiative heating from package 2 (Figs. 7b,c). In the second and third experiments, we only homogenize the convective heating (termed ConN) and the radiative heating (termed RadN), respectively, both to help explain the responses in the first experiment and to quantify the relative contributions of these individual heatings to the ITCZ in the southern Indian Ocean.

Figure 8 shows the annual mean net diabatic and dynamical[2] heating, respectively, averaged over the target region in the control and homogenization experiments. As expected, the annual mean diabatic (Fig. 8a) and dynamical (Fig. 8b) heating balance each other. The areal mean diabatic heating in the free troposphere (about 700–300 hPa) is positive (i.e., warming tendency) in CNTL, but in response to the homogenization of diabatic heating, it weakens significantly in RadN and ConN and even becomes negative in AllN. This weakening results from the dynamical adjustment of the atmosphere in response to the homogenization. Homogenization reduces the amplitude of the diabatic warming and cooling nearly everywhere over the target region and if the atmosphere thermodynamic structure remains largely unchanged (averaged over time; see explanations below), the circulation must weaken to balance the reduced diabatic heating. To illustrate that this is indeed what happens in the homogenization experiments, we zoom into the ITCZ region in the southern Indian Ocean (0°–10°S, 60°–90°E) and compare the areal mean diabatic heating, vertical velocity, air temperature, and humidity among the experiments (Fig. 9). In response to the homogenization, the diabatic heating averaged over this ITCZ region (Fig. 9a) shows similar changes to the areal mean over the target region (Fig. 8a), with significant weakening of the diabatic warming below about 200 hPa in all homogenization experiments and even reversing to diabatic cooling in ConN above about 500 hPa and in AllN above 700 hPa. Consistent with the changes in diabatic heating (and opposite-sign dynamical cooling; not shown), the ascent associated with the ITCZ convection (Fig. 9b) weakens significantly throughout the troposphere and becomes descent in ConN from 500 hPa to about 250 hPa and in AllN above about 650 hPa. In contrast, the vertical structure in both air temperature and humidity in all homogenization experiments remains similar to that in the control experiment (Figs. 9c,d). The weak changes in atmosphere thermodynamics result from the compensation between the reduced diabatic warming from homogenization over the ITCZ region and the weakened dynamical cooling associated with weakening ascent, which is consistent with the weak temperature gradients constraint in the topics (Sobel and Bretherton 2000; Sobel et al. 2001). The result that changes in ConN and RadN are similar can be explained by the fact that the convective heating and the radiative cooling in the control run have similar horizontal gradients; that is, their values increase from subsidence regions to ascent regions (cf. Figs. 7b and 7c). Homogenizing these two heatings is equivalent to imposing diabatic forcings that have similar spatial structure but mainly differ in amplitude (stronger in ConN). Therefore, the responses in all three homogenization experiments are similar in pattern but different in amplitude.

We further decompose the net diabatic heating over the ITCZ region in the southern Indian Ocean into the leading convective and radiative heating components. As shown in Fig. 10, it is clear that changes in the radiation are weak such that changes in the net diabatic heating are mostly achieved by changes in the convective heating in all the homogenization

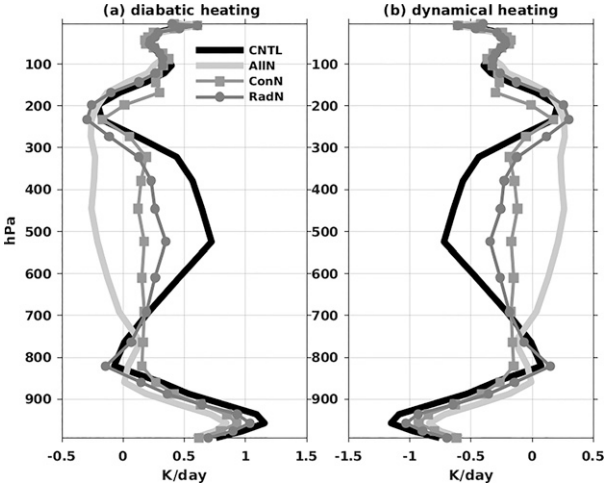

FIG. 8. Vertical profiles of the net (a) diabatic and (b) dynamical heating (K day^{-1}) in the CAM6 experiments averaged over the target region (20°S–30°N, 30°–120°E) where homogenization is implemented. The diabatic heating is diagnosed from physical parameterizations while the dynamical heating is diagnosed from the dynamical core. The legend in (a) denotes different experiments, with CNTL in heavy black, AllN in heavy gray, ConN in thin gray with squares, and RadN in thin gray with dots.

[2] Dynamical heating is the heating from a model's dynamical core, which contains the large-scale adiabatic part of the model (the discretized equations of motion) and is explicitly resolved on the underlying grid, whereas diabatic heating is the heating from physical parameterizations of subgrid-scale, diabatic processes.

Unauthenticated | Downloaded 12/07/22 10:48 PM UTC

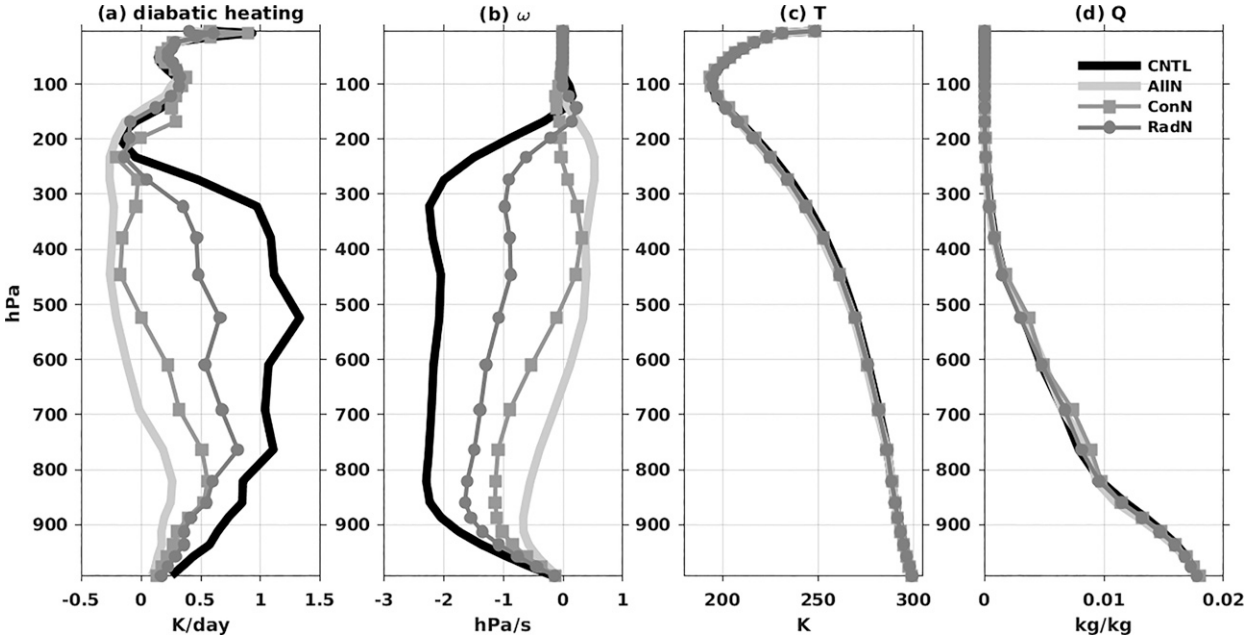

FIG. 9. Vertical profiles of (a) the net diabatic heating (K day^{-1}), (b) pressure velocity omega (hPa s^{-1}), (c) air temperature (K), and (d) specific humidity averaged over the southern Indian Ocean ITCZ region (10°S–0°, 60°–90°E) in the CAM6 experiments. The legend in (d) denotes different experiments, with CNTL in heavy black, AllN in heavy gray, ConN in thin gray with squares, and RadN in thin gray with dots.

experiments, including RadN where the radiative heating is homogenized directly. This result is consistent with the changes in atmosphere circulation and thermodynamic structure (Figs. 9b–d). The large changes in vertical velocity suggest large changes in convective heating, while the weak changes in atmosphere temperature and humidity mean that the radiative heating remains mostly unchanged.

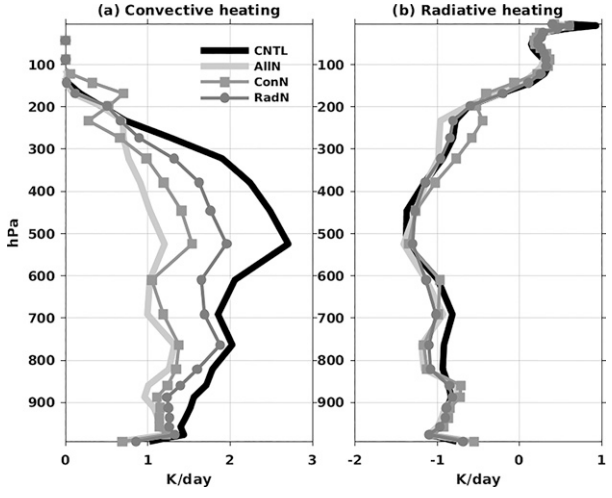

FIG. 10. Vertical profiles of the (a) convective and (b) radiative heating (K day^{-1}) averaged over the southern Indian Ocean ITCZ region (10°S–0°, 60°–90°E) in the CAM6 experiments. The legend in (a) denotes different experiments, with CNTL in heavy black, AllN in heavy gray, ConN in thin gray with squares, and RadN in thin gray with dots.

How does the ITCZ in the southern Indian Ocean respond to these changes in the free atmosphere? Figure 11 shows the precipitation, 993-hPa winds, and associated divergence in AllN and their differences from CNTL averaged during DJF and JJA, respectively. The spatial structure of these fields in AllN should be caused only by the imposed SST forcing through PBL processes (i.e., below 850 hPa), while the differences (CNTL − AllN) should be attributed to the impacts of the structured diabatic heating in the free atmosphere (i.e., above 850 hPa). In the southern Indian Ocean (about 0°–20°S), AllN still simulates broad surface convergence that, as in CNTL (Figs. 6a,c), results from the convergence of the northeast and southeast trade winds during DJF (Fig. 11a) and from the slowdown of the southeast trade winds during JJA (Fig. 11b) (attributable to the PBL processes). However, the amplitude in these seasonal mean winds and divergence is significantly weaker than in CNTL (Figs. 11c,d) (attributable to the free-atmosphere structured diabatic heating). Over the ITCZ in the southern Indian Ocean (0°–10°S), the precipitation is above 4 mm day^{-1} in both DJF and JJA in CNTL (Figs. 6a,c) but is mostly below 4 mm day^{-1} in AllN (Figs. 11a,b), such that the differences in precipitation (Figs. 11c,d) are more similar to the CNTL precipitation.

To further quantify the relative contributions of the PBL processes versus the free-atmosphere diabatic heating to the ITCZ in the Indian Ocean, we compute the percentage of the ITCZ precipitation (and surface convergence for which results are similar and not shown) in CTNL explained by each. Figures 12a and 12b show the contribution of the free-atmosphere structured diabatic heating, estimated as

Unauthenticated | Downloaded 12/07/22 10:48 PM UTC

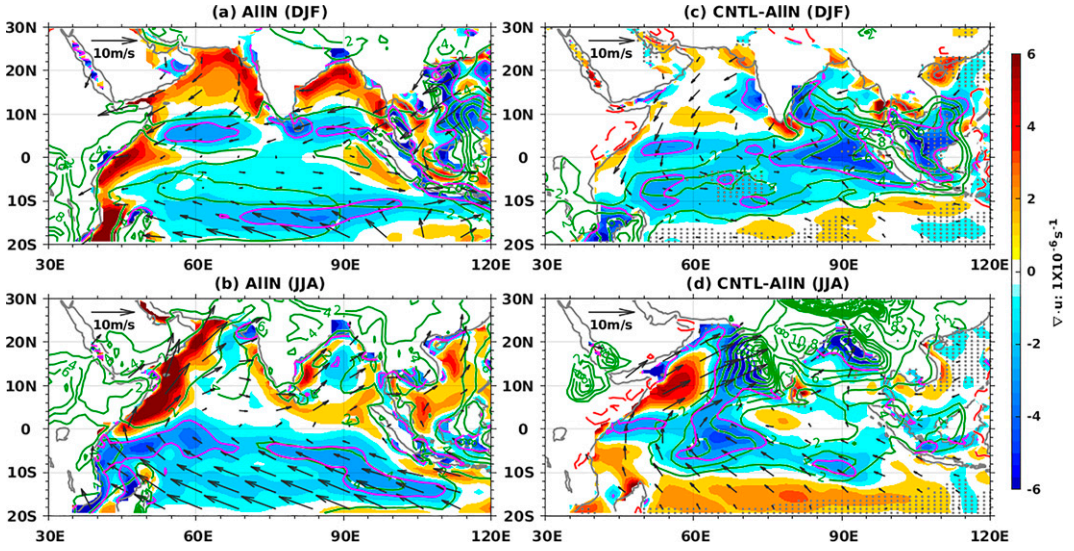

FIG. 11. DJF (a) and JJA (b) climatology of precipitation (green contours; mm day^{-1}), 993-hPa winds (vectors; m s^{-1}), and associated divergence (shading; 10^{-6} s^{-1}, with the -2×10^{-6} s^{-1} isoline highlighted in magenta contour) in AllN, in which the net diabatic heating above 850 hPa over the displayed region is homogenized. The surface spatial structure in AllN should be interpreted as a result of the imposed SST forcing through the PBL processes. Also shown in (c) DJF and (d) JJA are the corresponding differences, CNTL − AllN, which quantify the contributions of horizontal gradients in the free-troposphere diabatic heating to the surface spatial structure. Precipitation contours start at 2 mm day^{-1} and have an interval of 2 mm day^{-1}, with positive in green and negative in dashed red, in (c) and (d) only. A 10 m s^{-1} reference vector is shown in the upper-left corner of each panel. Stippling in (c) and (d) indicates that the difference is not significant at 5% level based on a two-sided *t* test.

$[P(\text{CNTL}) - P(\text{AllN})]/P(\text{CNTL}) \times 100\%$, where P denotes seasonal mean precipitation over regions where P is above 4 mm day^{-1} (the threshold in our ITCZ definition). The PBL contribution is simply the remaining percentage. During DJF (Fig. 12a), the free-atmosphere structured total diabatic heating contributes more than 60% to the ITCZ precipitation in the southern Indian Ocean and about 65% averaged over the central ITCZ region (0°–10°S, 60°–90°E, indicated by the black-dashed box in Fig. 12a); during JJA (Fig. 12b), it contributes around 50% to the southern ITCZ and about 48% averaged over the central ITCZ region. In general, the stronger mean precipitation in CNTL arises from the larger contribution from the free-atmosphere structured diabatic heating, a relationship also true for the SASM region during JJA (Fig. 12b).

We repeat the same assessment for the convective (ConN) and radiative (RadN) heating and summarize the contributions averaged over the central ITCZ region (0°–10°S, 60°–90°E) in Figs. 12c,d. During DJF, the structured convective heating and radiative heating in the free atmosphere contribute about 55% and 32% to the ITCZ precipitation over the southern Indian Ocean (0°–10°S, 60°–90°E), whereas during JJA they contribute about 27% and 38%. Compared to the contributions estimated from AllN, the contributions of the structured convective heating and radiative heating in the free atmosphere do not add up linearly, although these two heatings add up to the total diabatic heating. This likely indicates some nonlinear interactions between the free-atmosphere structured diabatic heating and convection over the ITCZ in the southern Indian Ocean. We have also conducted this analysis for the MAM and SON seasons (not shown here). The percentage contributions during SON are very similar to those during JJA. During MAM, the ITCZ over the southern Indian Ocean, weakest of the year, appears to be dominated by the PBL processes (61%) in CAM6. Taken together, stronger (weaker) mean precipitation in the control simulation arises from larger (smaller) contributions from the free-atmosphere structured diabatic heating, a relationship applicable to both the southern ITCZ and the northern monsoon in the Indian Ocean as well as other tropical rainy regions (based on the sensitivity experiment with homogenization over the entire tropics; not shown).

4. Summary and discussion

ITCZs and associated mechanisms have been explored previously in the zonal mean and the Pacific and the Atlantic Oceans, but less so in the Indian Ocean and especially rarely for the year-round ITCZ in the southern Indian Ocean. In this work, we investigate the southern Indian Ocean ITCZ in reanalysis products and observations from ships and satellites, a simple linear dynamical model, and a complex state-of-the-art AGCM. We take an atmosphere perspective and quantify how the observed SST drives the ITCZ in the Indian Ocean. Specifically, we focus on the relative roles of the PBL processes versus the free-atmosphere structured diabatic heating, a question that has been widely debated in literature and still not fully addressed.

Unauthenticated | Downloaded 12/07/22 10:48 PM UTC

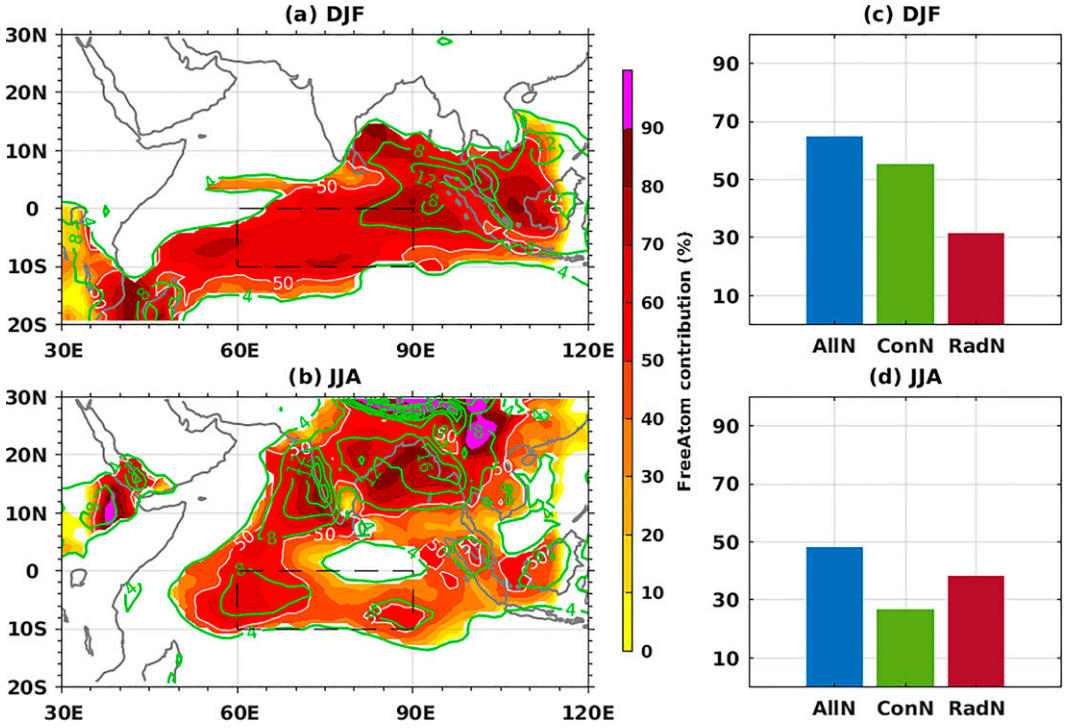

FIG. 12. Contribution (%) of the free-atmosphere structured diabatic heating to seasonal mean precipitation during (a),(c) DJF and (b),(d) JJA. The contribution is estimated as $[P(\text{CNTL}) - P(X)]/P(\text{CNTL}) \times 100\%$, where P denotes precipitation and X the homogenization experiment. In (a) and (b), shading shows results from AllN estimated over regions where the seasonal mean precipitation (green contours) from CNTL is above 4 mm day^{-1}; white contours indicate the 50% isolines. Bars in (c) and (d) show the contribution averaged over the central ITCZ region [0°–10°S, 60°–90°E, indicated by the black dashed box in (a) and (b)] from the total diabatic heating (AllN), convective heating (ConN), and radiative heating (RadN), respectively.

Various observational datasets show that the Indian Ocean has a robust ITCZ south of the equator year-round. This ITCZ migrates in the southern tropical Indian Ocean with a weak semiannual cycle. It peaks around January–February with strongest precipitation, southernmost location, and a northeast–southwest orientation from the Maritime Continent to Madagascar, reaches a minimum around May with a zonal orientation, grows until its secondary maximum around September with a northwest–southeast orientation, weakens slightly until December, and then regains its mature phase in January. During austral summer, this southern Indian Ocean ITCZ appears to be a typical ITCZ with converging trade winds from both hemispheres (similar to those in the Pacific and Atlantic), whereas during austral winter it appears to be a result of the slowdown of the cross-equatorial southeast trade winds. During austral winter the precipitation associated with the ITCZ in the southern Indian Ocean is secondary to the monsoonal precipitation in South Asia.

In reanalysis datasets, the ITCZ in the southern Indian Ocean during local summer exists over maximum surface moist static energy (and SST), which is consistent with the convective quasi-equilibrium theory. However, during boreal summer, the surface MSE maximizes in the northern summer monsoon region and decreases monotonically southward across the southern ITCZ region. Therefore, the convective quasi-equilibrium theory cannot explain the existence of the wintertime ITCZ in the southern Indian Ocean. A theory based on boundary layer momentum balance (Pauluis 2004), proposed for zonal mean circulation, could be relevant to the wintertime ITCZ in the southern Indian Ocean. This theory, known as the equatorial jump mechanism, argues that wintertime boundary layer winds can only cross the equator in the presence of a strong cross-equatorial pressure gradient (to overcome friction), which in the tropics arises mainly from gradients in SST owing to the weak pressure gradients in the free atmosphere. If there are no strong cross-equatorial gradients in SST, boundary layer trade winds have to rise in the wintertime hemisphere and cross the equator in the free atmosphere, which leads to a secondary precipitation maximum in the wintertime hemisphere. However, an examination of the meridional overturning circulation from the ERA reanalysis does not support the relevance of the equatorial jump mechanism to the southern ITCZ in the Indian Ocean (Fig. 13). During austral winter (JJA), the southeast trade winds cross the equator within the boundary layer below about 800 hPa (despite the rather weak cross-equatorial SST gradients, Fig. 4d); above 800 hPa in the free troposphere, the reanalysis product does not exhibit any noticeable cross-equatorial winds but

Unauthenticated | Downloaded 12/07/22 10:48 PM UTC

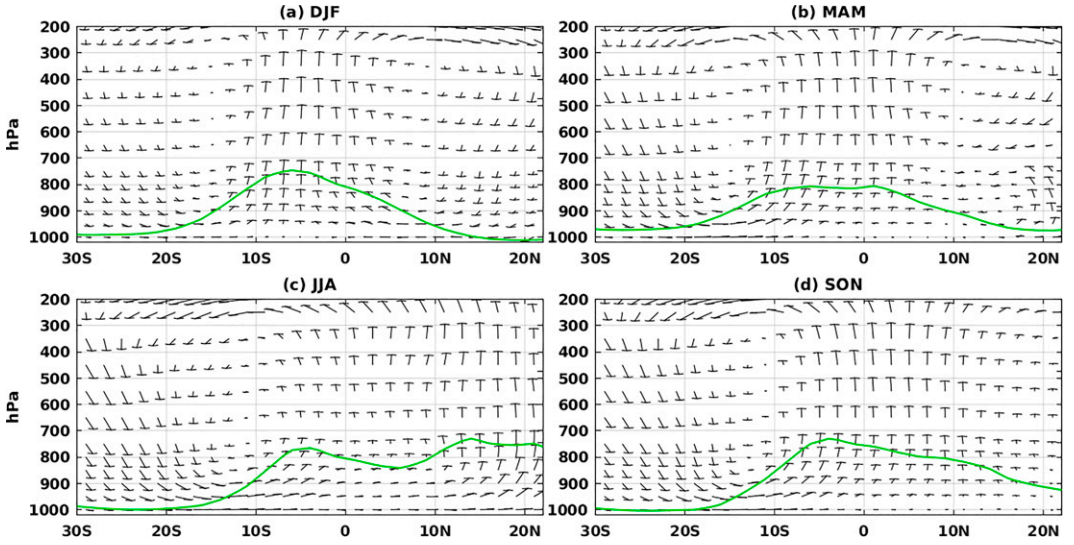

FIG. 13. Meridional overturning circulation averaged over the Indian Ocean from 70° to 100°E in the ERA. Vectors show $\langle v, \omega \times 2 \times 10^3 \rangle$ (ω is amplified by 2×10^3 in order to better display the vertical motion). The green contour qualitatively illustrates the distribution of the CMAP precipitation. Seasonal averages are shown for (a) DJF, (b) MAM, (c) JJA, and (d) SON.

ascent. In addition, Nie et al. (2010) in their analysis of the monsoon on the Indian Ocean sector also present flow diagrams that do not show the jump (see their Fig. 7a). Therefore, neither the convective quasi-equilibrium theory nor the equatorial jump mechanism can explain the existence of the ITCZ in the southern Indian Ocean during austral winter.

We turn to numerical models to further investigate and quantify the mechanisms underlying the ITCZ in the southern Indian Ocean, taking the observed SST as given. A linear dynamical model, interpretable as either a Lindzen–Nigam boundary layer model or a Gill-type free-atmosphere model, has high skill in simulating the ITCZ in the southern Indian Ocean during all seasons when forced by observed virtual surface temperature. The linear model captures well the location of the ITCZ in the southern Indian Ocean as well as its changing orientations among different seasons. The main biases lie in the amplitude of the low-level wind convergence, which tends to maximize closer to the equator than in nature. These successes and failures of the linear model in the Indian Ocean are consistent with previous studies using similar models to simulate the ITCZs in the Pacific and Atlantic (e.g., Back and Bretherton 2009b; Adam 2018). Considering the historical debates around the physical interpretations of the linear model [see reviews by Wang and Li (1993) and Sobel (2007)], these results cannot be attributed to either the PBL dynamics (as intended by the Lindzen–Nigam model) or the free-atmosphere processes (as intended by the Gill-type model).

A state-of-the-art AGCM, CAM6, hence is used to further address the relative contributions of the PBL and free-atmosphere processes to the ITCZ in the southern Indian Ocean. Driven by observed SST and sea ice, CAM6 realistically simulates the ITCZ in the southern Indian Ocean in terms of both surface winds and precipitation (albeit with noticeable biases in amplitude). Perturbation experiments are designed to isolate the contributions of the PBL processes by removing the impacts of the free-atmosphere structured diabatic heating. This is done by horizontally homogenizing on isobaric surfaces the model-computed diabatic heating at every model time step over the Indian Ocean in the free atmosphere before passing onto the thermodynamic equation. This is implemented to conserve the areal mean heating in the homogenization region. Since the homogenization is expected to impact the atmosphere both inside and outside the Indian Ocean (owing to the weak temperature gradient constraint in the tropical free atmosphere), we further nudge the horizontal winds and temperature outside the homogenization region back toward the control simulation to isolate the impact of the changes within the Indian Ocean.

Homogenizing the free-atmosphere structured diabatic heating essentially reduces the amplitude of the diabatic warming and cooling nearly everywhere in the Indian Ocean. As a result, the steady response is a weakening in the free-atmosphere circulation, with stronger weakening over regions where the diabatic heating in the control run is larger. This dynamical adjustment largely offsets the imposed homogenization, which results in weak changes in atmosphere temperature and humidity and thus weak changes in radiation. So averaged over time, the homogenization of the free-atmosphere total diabatic heating mainly leads to large weakening in convective heating and circulation, but not in atmosphere thermodynamics and radiation. Similar but weaker responses are obtained when homogenizing the convective and radiative heating separately. This similarity in response stems from the similar horizontal structure in these individual (and thus the total) diabatic heatings, with their values increasing from subsidence regions to ascent regions.

Unauthenticated | Downloaded 12/07/22 10:48 PM UTC

Despite the lack of structured diabatic heating in the free atmosphere, the surface wind convergence and precipitation associated with the ITCZ in the southern Indian Ocean still exist year-round, owing to the imposed SST through the PBL processes (e.g., the SST-driven pressure gradients). However, the wind convergence and precipitation over the ITCZ region weaken significantly and the surface convergence expands farther poleward (where SST gradients are stronger). These changes suggest a significant contribution from the free-atmosphere structured diabatic heating. Quantified by precipitation (and surface convergence) averaged over the central ITCZ region (0°–10°S, 60°–90°E), the contribution of total diabatic heating in the free-atmosphere ranges from about 40% during austral fall (MAM, the weakest phase of the ITCZ) to about 50% during austral winter and spring (June to November) and to about 70% during austral summer (DJF, the peak phase of the ITCZ). The conclusion is that, in CAM6 driven by the observed SST, the year-round ITCZ in the southern Indian Ocean owns its existence to the PBL processes, and owns its strength to both the PBL processes and the free-atmosphere structured diabatic heating. Their contributions to the ITCZ strength are comparable during austral winter and spring; during austral fall when the ITCZ in the southern Indian Ocean is in its weakest phase, the PBL processes contribute about 60%, whereas during austral summer when the ITCZ is in its mature phase, the free-atmosphere structured diabatic heating dominates by about 70%. In CAM6, the dominant contribution of the free-atmosphere diabatic heating to peaks in rainfall and surface convergence over the southern Indian Ocean also holds true for the rest of the rainy regions in the tropics (including both ITCZ and monsoonal regions).

Concerning the relative contributions of the PBL processes versus free-atmosphere diabatic heating on the surface, our quantitative conclusions derived from the Indian Ocean ITCZ appear to disagree with previous findings by Chiang et al. (2001) on the Pacific ITCZ and Back and Bretherton (2009a,b) on the general ITCZs. Based either on linear models or idealized empirical models, these previous studies found that deep convective heating dominates the surface zonal winds while the SST-driven PBL pressure gradients dominate the surface meridional winds and convergence. However, our results from CAM6 show that the SST-driven PBL gradients and free-atmosphere diabatic heating can both drive significant zonal and meridional winds at the surface in the Indian Ocean and that it is the free-atmosphere diabatic heating that dominates the amplitude of the surface convergence during the mature-phase ITCZ (Fig. 11). The reasons for these disagreements are hard to diagnose considering the differences in the models used and the regions focused on. Nonetheless, our conclusions derived from climatology are consistent with recent observation-based studies focusing on climate variability on intraseasonal to interannual time scales, such as the Madden–Julian oscillation (MJO) and ENSO. For example, on intraseasonal time scales, strong surface winds near the eastward-moving center of deep convection during MJO events are considered to be driven largely by the associated convective heating and this relationship is stronger during local summer [see a review by Zhang (2005) and the references therein; Adames and Kim 2016]. This is consistent with our finding that the free-atmosphere diabatic heating dominates the strength of surface wind convergence associated with the ITCZs and monsoons during their mature phase.

The year-round ITCZ south of the equator in the Indian Ocean is unique compared to the prevalent Northern Hemisphere ITCZs in the tropical oceans. Explaining this unique southern Indian Ocean ITCZ requires an account of not only the associated atmospheric processes given observed SSTs but also the processes shaping the observed SST distribution. This work focuses on the first part of the question. The second part will be addressed in the future with fully coupled models that also include active ocean dynamics.

Acknowledgments. This work was supported by the NSF Awards AGS 19-34363 and 19-34392. We thank Steve Goldhaber and Patrick Callaghan for their help with the CAM6 experiments. Discussions with Adam Sobel and Michela Biasutti and comments from anonymous reviewers are greatly appreciated. We acknowledge the various datasets that made this analysis possible: ICOADS (https://icoads.noaa.gov/), satellite observations of high cloud fraction from the GCM-Oriented Cloud CALIPSO Product (GOCCP; https://climserv.ipsl.polytechnique.fr/cfmip-obs/Calipso_goccp.html) and outgoing longwave radiation from the Clouds and the Earth's Radiant Energy System (CERES) Energy Balanced and Filled (EBAF) Edition 4.1 (https://ceres.larc.nasa.gov/data/), the CMAP and GPCP precipitation and the NCEP–DOE reanalysis II winds from NOAA/OAR/ESRL PSL, Boulder, Colorado, USA (https://psl.noaa.gov/data/gridded), and the ERA5 reanalysis from ECMWF (https://www.ecmwf.int/en/forecasts/datasets/reanalysis-datasets/era5).

Data availability statement. All data used in this work are available upon request to the corresponding author.

APPENDIX A

Derivation of the Lindzen–Nigam Model for Total Field

In the Lindzen–Nigam model, the equations for zonal mean (indicated by an overbar) and eddy component (indicated by a prime) can be expressed in Cartesian coordinates as follows:

$$\begin{cases} \varepsilon\overline{u} - f\overline{v} = 0, \\ \varepsilon\overline{v} + f\overline{u} + g\left(2 - \dfrac{\overline{T}_s}{T_0} + \dfrac{\alpha H_0}{T_0}\right)\dfrac{\partial\overline{h}}{\partial y} = \dfrac{gH_0}{2T_0}\dfrac{\partial\overline{T}_s}{\partial y}, \\ \overline{h} + \tau_c H_0\dfrac{\partial\overline{v}}{\partial y} = 0, \end{cases}$$

$$\begin{cases} \varepsilon u' - fv' + g\left(2 - \dfrac{\overline{T}_s}{T_0} + \dfrac{\alpha H_0}{T_0}\right)\dfrac{\partial h'}{\partial x} = \dfrac{gH_0}{2T_0}\left(1 - \dfrac{2}{3}\gamma\right)\dfrac{\partial T_s'}{\partial x}, \\ \varepsilon v' + fu' + g\left(2 - \dfrac{\overline{T}_s}{T_0} + \dfrac{\alpha H_0}{T_0}\right)\dfrac{\partial h'}{\partial y} = \dfrac{gH_0}{2T_0}\left(1 - \dfrac{2}{3}\gamma\right)\dfrac{\partial T_s'}{\partial y} + \dfrac{gh'}{2T_0}\dfrac{\partial\overline{T}_s}{\partial y}, \\ h' + \tau_c H_0\left(\dfrac{\partial u'}{\partial x} + \dfrac{\partial v'}{\partial y}\right) = 0, \end{cases}$$

Unauthenticated | Downloaded 12/07/22 10:48 PM UTC

where u and v are the mass-weighted horizontal winds vertically averaged through the depth of the PBL, h is the perturbation in the PBL height, T_s is the prescribed surface temperature, f is the Coriolis parameter, and g is the gravitational acceleration. Other parameters and their values used in Lindzen and Nigam (1987) include $T_0 = 288$ K (a reference temperature for linearization), $H_0 = 3$ km (the mean depth of the PBL), $\alpha = 0.003$ K m^{-1} (the lapse rate of zonal mean temperature), $\gamma = 0.3$ (a parameter controlling the lapse rate of eddy temperature), $\tau_c = 30$ minutes (the adjustment time for the PBL height as cumulus convection responds to boundary layer convergence), and $\varepsilon = (2.5 \text{ days})^{-1}$ (the Rayleigh friction coefficient).

Neglecting the smaller terms [those related with γ and $(gh'/2T_0)(\partial\overline{T}_s/\partial y)$] and setting $\overline{T}_s = 297$K (such that $2 - \overline{T}_s/T_0 + \alpha H_0/T_0 = 1$) (Neelin 1989), the resulting equations have the same form for the zonal mean and eddy components (note that $\partial\overline{h}/\partial x = \partial\overline{T}_s/\partial x = \partial\overline{u}_s/\partial x = 0$ by definition and have been added to the zonal mean equations):

$$\begin{cases} \varepsilon\overline{u} - f\overline{v} + g\dfrac{\partial\overline{h}}{\partial x} = \dfrac{gH_0}{2T_0}\dfrac{\partial\overline{T}_s}{\partial x}, \\ \varepsilon\overline{v} + f\overline{u} + g\dfrac{\partial\overline{h}}{\partial y} = \dfrac{gH_0}{2T_0}\dfrac{\partial\overline{T}_s}{\partial y}, \\ \overline{h} + \tau_c H_0\left(\dfrac{\partial\overline{u}}{\partial x} + \dfrac{\partial\overline{v}}{\partial y}\right) = 0, \end{cases}$$

$$\begin{cases} \varepsilon u' - fv' + g\dfrac{\partial h'}{\partial x} = \dfrac{gH_0}{2T_0}\dfrac{\partial T_s'}{\partial x}, \\ \varepsilon v' + fu' + g\dfrac{\partial h'}{\partial y} = \dfrac{gH_0}{2T_0}\dfrac{\partial T_s'}{\partial y}, \\ h' + \tau_c H_0\left(\dfrac{\partial u'}{\partial x} + \dfrac{\partial v'}{\partial y}\right) = 0. \end{cases}$$

Adding them up yields the equations for the total field:

$$\begin{cases} \varepsilon u - fv + g\dfrac{\partial h}{\partial x} = \dfrac{gH_0}{2T_0}\dfrac{\partial T_s}{\partial x}, \\ \varepsilon v + fu + g\dfrac{\partial h}{\partial y} = \dfrac{gH_0}{2T_0}\dfrac{\partial T_s}{\partial y}, \\ h + \tau_c H_0\left(\dfrac{\partial u}{\partial x} + \dfrac{\partial v}{\partial y}\right) = 0. \end{cases}$$

Defining a new variable $\hbar \equiv h - (H_0/2T_0)T_s$, we get

$$\begin{cases} \varepsilon u - fv + g\dfrac{\partial\hbar}{\partial x} = 0, \\ \varepsilon v + fu + g\dfrac{\partial\hbar}{\partial y} = 0, \\ \varepsilon_T\hbar + H_0\left(\dfrac{\partial u}{\partial x} + \dfrac{\partial v}{\partial y}\right) = -Q. \end{cases}$$

where $Q = (H_0/2T_0\tau_c)T_s$ and $\varepsilon_T = 1/\tau_c$. This set of equations has the same form as that in the Gill model (Gill 1980).

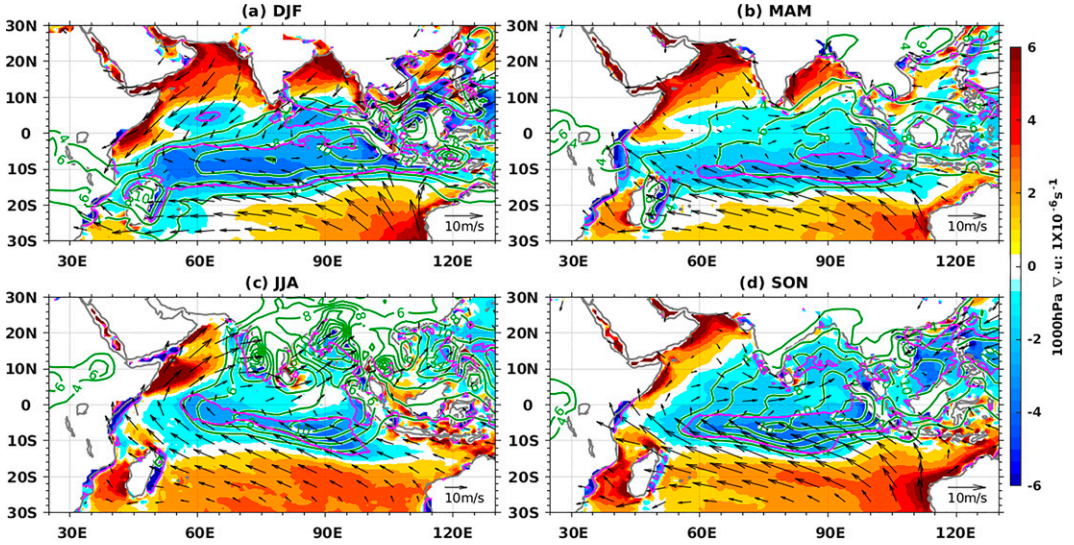

FIG. B1. Seasonal climatology of the CAM6 precipitation (green contours; mm day^{-1}), the ERA5 1000-hPa winds (vectors; m s^{-1}), and divergence (shading; 10^{-6} s^{-1}, with the -2×10^{-6} s^{-1} isoline highlighted in magenta contour), for (a) DJF, (b) MAM, (c) JJA, and (d) SON. Precipitation contours start at 4 mm day^{-1} and increase every 2 mm day^{-1}. A 10 m s^{-1} reference vector is shown in the lower-right corner of each panel. This figure shows the seasonal mean of the data in Fig. 1 and is intended to compare directly with the CAM6 simulation in Fig. 6.

Unauthenticated | Downloaded 12/07/22 10:48 PM UTC

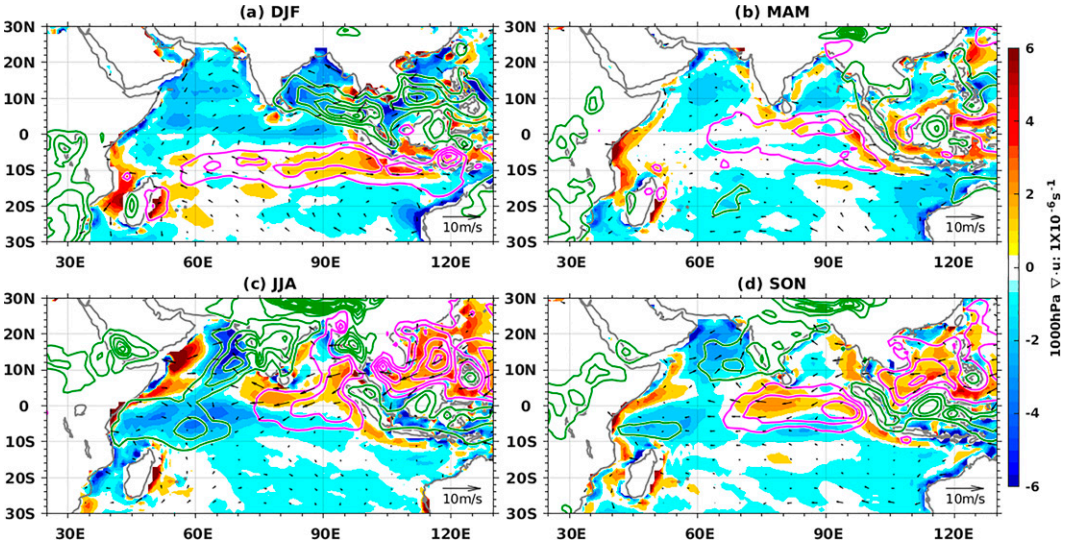

FIG. B2. CAM6 biases estimated as the difference between Fig. 6 and Fig. B1 (model minus data). The green (magenta) contours indicate stronger (weaker) precipitation in CAM6 than CMAP. Contours start at ±2 mm day^{-1} and increase every ±2 mm day^{-1}. The winds (vectors) and divergence (shading) difference is estimated between the lowest model level of 993 hPa and observed at 1000 hPa.

APPENDIX B

CAM6 Evaluation

This section evaluates the performance of CAM6 in simulating the Indian Ocean ITCZ. Figure B1 shows the seasonal mean of the data in Fig. 1 and is intended to compare directly with the CAM6 simulation in Fig. 6. Figure B2 shows the biases in CAM6.

REFERENCES

Adam, O., 2018: Zonally varying ITCZs in a Matsuno-Gill-type model with an idealized Bjerknes feedback. *J. Adv. Model. Earth Syst.*, **10**, 1304–1318, https://doi.org/10.1029/2017MS001183.

——, T. Bischoff, and T. Schneider, 2016: Seasonal and interannual variations of the energy flux equator and ITCZ. Part II: Zonally varying shifts of the ITCZ. *J. Climate*, **29**, 7281–7293, https://doi.org/10.1175/JCLI-D-15-0710.1.

——, T. Schneider, and F. Brient, 2018: Regional and seasonal variations of the double-ITCZ bias in CMIP5 models. *Climate Dyn.*, **51**, 101–117. https://doi.org/10.1007/s00382-017-3909-1.

Adames, Á. F., and D. Kim, 2016: The MJO as a dispersive, convectively coupled moisture wave: Theory and observations. *J. Atmos. Sci.*, **73**, 913–941, https://doi.org/10.1175/JAS-D-15-0170.1.

Arakawa, A., and W. H. Schubert, 1974: Interaction of a cumulus cloud ensemble with the large-scale environment, part I. *J. Atmos. Sci.*, **31**, 674–701, https://doi.org/10.1175/1520-0469(1974)031<0674:IOACCE>2.0.CO;2.

Back, L. E., and C. S. Bretherton, 2009a: On the relationship between SST gradients, boundary layer winds, and convergence over the tropical oceans. *J. Climate*, **22**, 4182–4196, https://doi.org/10.1175/2009JCLI2392.1.

——, and ——, 2009b: A simple model of climatological rainfall and vertical motion patterns over the tropical oceans. *J. Climate*, **22**, 6477–6497, https://doi.org/10.1175/2009JCLI2393.1.

Biasutti, M., and Coauthors, 2018: Global energetics and local physics as drivers of past, present and future monsoons. *Nat. Geosci.*, **11**, 392–400, https://doi.org/10.1038/s41561-018-0137-1.

Bogenschutz, P. A., A. Gettelman, H. Morrison, V. E. Larson, C. Craig, and D. P. Schanen, 2013: Higher-order turbulence closure and its impact on climate simulations in the community atmosphere model. *J. Climate*, **26**, 9655–9676, https://doi.org/10.1175/JCLI-D-13-00075.1.

Boos, W. R., and R. L. Korty, 2016: Regional energy budget control of the intertropical convergence zone and application to mid-Holocene rainfall. *Nat. Geosci.*, **9**, 892–897, https://doi.org/10.1038/ngeo2833.

Broccoli, A. J., K. A. Dahl, and R. J. Stouffer, 2006: Response of the ITCZ to Northern Hemisphere cooling. *Geophys. Res. Lett.*, **33**, L01702, https://doi.org/10.1029/2005GL024546.

Byrne, M. P., A. G. Pendergrass, A. D. Rapp, and K. R. Wodzicki, 2018: Response of the intertropical convergence zone to climate change: Location, width, and strength. *Curr. Climate Change Rep.*, **4**, 355–370, https://doi.org/10.1007/s40641-018-0110-5.

Cabré, A., I. Marinov, and A. Gnanadesikan, 2017: Global atmospheric teleconnections and multidecadal climate oscillations driven by Southern Ocean convection. *J. Climate*, **30**, 8107–8126, https://doi.org/10.1175/JCLI-D-16-0741.1.

Chang, P., and Coauthors, 2006: Climate fluctuations of tropical coupled system: The role of ocean dynamics. *J. Climate*, **19**, 5122–5174, https://doi.org/10.1175/JCLI3903.1.

Chiang, J. C. H., and D. J. Vimont, 2004: Analogous Pacific and Atlantic meridional modes of tropical atmosphere–ocean variability. *J. Climate*, **17**, 4143–4158, https://doi.org/10.1175/JCLI4953.1.

——, S. E. Zebiak, and M. A. Cane, 2001: Relative roles of elevated heating and surface temperature gradients in driving

Unauthenticated | Downloaded 12/07/22 10:48 PM UTC

anomalous surface winds over tropical oceans. **58**, 1371–1394, https://doi.org/10.1175/1520-0469(2001)058<1371:RROEHA>2.0.CO;2.

Danabasoglu, G., and Coauthors, 2020: The Community Earth System Model version 2 (CESM2). *J. Adv. Model. Earth Syst.*, **12**, e2019MS001916, https://doi.org/10.1029/2019MS001916.

Donohoe, A., J. Marshall, D. Ferreira, and D. McGee, 2012: The relationship between ITCZ location and cross-equatorial atmospheric heat transport: From the seasonal cycle to the last glacial maximum. *J. Climate*, **26**, 3597–3618, https://doi.org/10.1175/JCLI-D-12-00467.1.

Emanuel, K. A., J. D. Neelin, and C. S. Bretherton, 1994: On large-scale circulations in convecting atmospheres. *Quart. J. Roy. Meteor. Soc.*, **120**, 1111–1143, https://doi.org/10.1002/qj.49712051902.

Freeman, E., and Coauthors, 2017: ICOADS release 3.0: A major update to the historical marine climate record. *Int. J. Climatol.*, **37**, 2211–2232, https://doi.org/10.1002/joc.4775.

Frierson, D. M. W., and Coauthors, 2013: Contribution of ocean overturning circulation to tropical rainfall peak in the Northern Hemisphere. *Nat. Geosci.*, **6**, 940–944, https://doi.org/10.1038/ngeo1987.

Gadgil, S., 2018: The monsoon system: Land–sea breeze or the ITCZ? *J. Earth Syst. Sci.*, **127** (1), 1, https://doi.org/10.1007/s12040-017-0916-x.

Geen, R., S. Bordoni, D. S. Battisti, and K. Hui, 2020: Monsoons, ITCZs, and the concept of the global monsoon. *Rev. Geophys.*, **58**, e2020RG000700, https://doi.org/10.1029/2020RG000700.

Gill, A. E., 1980: Some simple solutions for heat-induced tropical circulation. *Quart. J. Roy. Meteor. Soc.*, **106**, 447–462, https://doi.org/10.1002/qj.49710644905.

Golaz, J.-C., V. E. Larson, and W. R. Cotton, 2002: A PDF-based model for boundary layer clouds. Part I: Method and model description. *J. Atmos. Sci.*, **59**, 3540–3551, https://doi.org/10.1175/1520-0469(2002)059<3540:APBMFB>2.0.CO;2.

Hersbach, H., and Coauthors, 2020: The ERA5 global reanalysis. *Quart. J. Roy. Meteor. Soc.*, **146**, 1999–2049, https://doi.org/10.1002/qj.3803.

Hwang, Y.-T., and D. M. W. Frierson, 2010: Increasing atmospheric poleward energy transport with global warming. *Geophys. Res. Lett.*, **37**, L24807, https://doi.org/10.1029/2010GL045440.

——, and ——, 2013: Link between the double-Intertropical Convergence Zone problem and cloud biases over the Southern Ocean. *Proc. Natl. Acad. Sci. USA*, **110**, 4935–4940, https://doi.org/10.1073/pnas.1213302110.

Kang, S. M., and I. M. Held, 2012: Tropical precipitation, SSTs and the surface energy budget: A zonally symmetric perspective. *Climate Dyn.*, **38**, 1917–1924, https://doi.org/10.1007/s00382-011-1048-7.

——, and S.-P. Xie, 2014: Dependence of climate response on meridional structure of external thermal forcing. *J. Climate*, **27**, 5593–5600, https://doi.org/10.1175/JCLI-D-13-00622.1.

——, I. M. Held, D. M. W. Frierson, and M. Zhao, 2008: The response of the ITCZ to extratropical thermal forcing: Idealized slab-ocean experiments with a GCM. *J. Climate*, **21**, 3521–3532, https://doi.org/10.1175/2007JCLI2146.1.

——, Y. Shin, and S.-P. Xie, 2018: Extratropical forcing and tropical rainfall distribution: Energetics framework and ocean Ekman advection. *npj Climate Atmos. Sci.*, **1**, 2, https://doi.org/10.1038/s41612-017-0004-6.

Keshtgar, B., O. Alizadeh-Choobari, and P. Irannejad, 2020: Seasonal and interannual variations of the intertropical convergence zone over the Indian Ocean based on an energetic perspective. *Climate Dyn.*, **54**, 3627–3639, https://doi.org/10.1007/s00382-020-05195-5.

Levine, X. J., and W. R. Boos, 2017: Land surface albedo bias in climate models and its association with tropical rainfall. *Geophys. Res. Lett.*, **44**, 6363–6372, https://doi.org/10.1002/2017GL072510.

Li, G., and S.-P. Xie, 2014: Tropical biases in CMIP5 multimodel ensemble: The excessive equatorial Pacific cold tongue and double ITCZ problems. *J. Climate*, **27**, 1765–1780, https://doi.org/10.1175/JCLI-D-13-00337.1.

Lin, J.-L., 2007: The double-ITCZ problem in IPCC AR4 coupled GCMs: Ocean–atmosphere feedback analysis. *J. Climate*, **20**, 4497–4525, https://doi.org/10.1175/JCLI4272.1.

Lindzen, R. S., and S. Nigam, 1987: On the role of sea surface temperature gradients in forcing low-level winds and convergence in the tropics. *J. Atmos. Sci.*, **44**, 2418–2436, https://doi.org/10.1175/1520-0469(1987)044<2418:OTROSS>2.0.CO;2.

Loeb, N. G., and Coauthors, 2018: Clouds and the Earth's Radiant Energy System (CERES) Energy Balanced and Filled (EBAF) Top-of-Atmosphere (TOA) edition-4.0 data product. *J. Climate*, **31**, 895–918, https://doi.org/10.1175/JCLI-D-17-0208.1.

Marshall, J., A. Donohoe, D. Ferreira, and D. McGee, 2014: The ocean's role in setting the mean position of the inter-tropical convergence zone. *Climate Dyn.*, **42**, 1967–1979, https://doi.org/10.1007/s00382-013-1767-z.

Mitchell, T. P., and J. M. Wallace, 1992: The annual cycle in equatorial convection and sea surface temperature. *J. Climate*, **5**, 1140–1156, https://doi.org/10.1175/1520-0442(1992)005<1140:TACIEC>2.0.CO;2.

Neelin, J. D., 1989: On the interpretation of the Gill model. *J. Atmos. Sci.*, **46**, 2466–2468, https://doi.org/10.1175/1520-0469(1989)046<2466:OTIOTG>2.0.CO;2.

——, and I. M. Held, 1987: Modeling tropical convergence based on the moist static energy budget. *Mon. Wea. Rev.*, **115**, 3–12, https://doi.org/10.1175/1520-0493(1987)115<0003:MTCBOT>2.0.CO;2.

Nie, J., W. R. Boos, and Z. Kuang, 2010: Observational evaluation of a convective quasi-equilibrium view of monsoons. *J. Climate*, **23**, 4416–4428, https://doi.org/10.1175/2010JCLI3505.1.

Pauluis, O., 2004: Boundary layer dynamics and cross-equatorial Hadley circulation. *J. Atmos. Sci.*, **61**, 1161–1173, https://doi.org/10.1175/1520-0469(2004)061<1161:BLDACH>2.0.CO;2.

Philander, S. G. H., D. Gu, G. Lambert, T. Li, D. Halpern, N.-C. Lau, and R. C. Pacanowski, 1996: Why the ITCZ is mostly north of the equator. *J. Climate*, **9**, 2958–2972, https://doi.org/10.1175/1520-0442(1996)009<2958:WTIIMN>2.0.CO;2.

Popp, M., and N. J. Lutsko, 2017: Quantifying the zonal-mean structure of tropical precipitation. *Geophys. Res. Lett.*, **44**, 9470–9478, https://doi.org/10.1002/2017GL075235.

Potter, S. F., E. J. Dawson, and D. M. W. Frierson, 2017: Southern African orography impacts on low clouds and the Atlantic ITCZ in a coupled model. *Geophys. Res. Lett.*, **44**, 3283–3289, https://doi.org/10.1002/2017GL073098.

Privé, N. C., and R. A. Plumb, 2007: Monsoon dynamics with interactive forcing. Part I: Axisymmetric studies. *J. Atmos. Sci.*, **64**, 1417–1430, https://doi.org/10.1175/JAS3916.1.

Rodwell, M. J., and B. J. Hoskins, 2001: Subtropical anticyclones and summer monsoons. *J. Climate*, **14**, 3192–3211, https://doi.org/10.1175/1520-0442(2001)014<3192:SAASM>2.0.CO;2.

Schneider, T., T. Bischoff, and G. H. Haug, 2014: Migrations and dynamics of the intertropical convergence zone. *Nature*, **513**, 45–53, https://doi.org/10.1038/nature13636.

Unauthenticated | Downloaded 12/07/22 10:48 PM UTC

Seager, R., M. Cane, N. Henderson, D.-E. Lee, R. Abernathey, and H. Zhang, 2019: Strengthening tropical Pacific zonal sea surface temperature gradient consistent with rising greenhouse gases. *Nat. Climate Change*, **9**, 517–522, https://doi.org/10.1038/s41558-019-0505-x.

Sobel, A. H., 2007: Simple models of ensemble-averaged precipitation and surface wind, given the sea surface temperature. *The Global Circulation of the Atmosphere*, T. Schneider and A. H. Sobel, Eds., Princeton University Press, 219–251.

——, and C. S. Bretherton, 2000: Modeling tropical precipitation in a single column. *J. Climate*, **13**, 4378–4392, https://doi.org/10.1175/1520-0442(2000)013<4378:MTPIAS>2.0.CO;2.

——, J. Nilsson, and L. M. Polvani, 2001: The weak temperature gradient approximation and balanced tropical moisture waves. *J. Atmos. Sci.*, **58**, 3650–3665, https://doi.org/10.1175/1520-0469(2001)058<3650:TWTGAA>2.0.CO;2.

Song, F., and G. J. Zhang, 2016: Effects of southeastern Pacific sea surface temperature on the double-ITCZ bias in NCAR CESM1. *J. Climate*, **29**, 7417–7433, https://doi.org/10.1175/JCLI-D-15-0852.1.

Takahashi, K., and D. S. Battisti, 2007: Processes controlling the mean tropical Pacific precipitation pattern. Part I: The Andes and the eastern Pacific ITCZ. *J. Climate*, **20**, 3434–3451, https://doi.org/10.1175/JCLI4198.1.

Timmermann, A., and Coauthors, 2018: El Niño–Southern Oscillation complexity. *Nature*, **559**, 535–545, https://doi.org/10.1038/s41586-018-0252-6.

Titchner, H. A., and N. A. Rayner, 2014: The Met Office Hadley Centre sea ice and sea surface temperature data set, version 2: 1. Sea ice concentrations: HadISST sea ice concentrations. *J. Geophys. Res.*, **119**, 2864–2889, https://doi.org/10.1002/2013JD020316.

Tomassini, L., 2020: The interaction between moist convection and the atmospheric circulation in the tropics. *Bull. Amer. Meteor. Soc.*, **101**, E1378–E1396, https://doi.org/10.1175/BAMS-D-19-0180.1.

Wang, B., and T. Li, 1993: A simple tropical atmosphere model of relevance to short-term climate variations. *J. Atmos. Sci.*, **50**, 260–284, https://doi.org/10.1175/1520-0469(1993)050<0260:ASTAMO>2.0.CO;2.

Winker, D. M., M. A. Vaughan, A. Omar, Y. Hu, K. A. Powell, Z. Liu, W. H. Hunt, and S. A. Young, 2009: Overview of the CALIPSO mission and CALIOP data processing algorithms. *J. Atmos. Oceanic Technol.*, **26**, 2310–2323, https://doi.org/10.1175/2009JTECHA1281.1.

Wu, Z., E. S. Sarachik, and D. S. Battisti, 1999: Thermally forced surface winds on an equatorial beta plane. *J. Atmos. Sci.*, **56**, 2029–2037, https://doi.org/10.1175/1520-0469(1999)056<2029:TFSWOA>2.0.CO;2.

——, ——, and ——, 2000: Vertical structure of convective heating and the three-dimensional structure of the forced circulation on an equatorial beta plane. *J. Atmos. Sci.*, **57**, 2169–2187, https://doi.org/10.1175/1520-0469(2000)057<2169:VSOCHA>2.0.CO;2.

Xiang, B., M. Zhao, I. M. Held, and J.-C. Golaz, 2017: Predicting the severity of spurious "double ITCZ" problem in CMIP5 coupled models from AMIP simulations. *Geophys. Res. Lett.*, **44**, 1520–1527, https://doi.org/10.1002/2016GL071992.

Xie, P., and P. A. Arkin, 1997: Global precipitation: A 17-year monthly analysis based on gauge observations, satellite estimates, and numerical model outputs. *Bull. Amer. Meteor. Soc.*, **78**, 2539–2558, https://doi.org/10.1175/1520-0477(1997)078<2539:GPAYMA>2.0.CO;2.

Xie, S.-P., 1996: Westward propagation of latitudinal asymmetry in a coupled ocean–atmosphere model. *J. Atmos. Sci.*, **53**, 3236–3250, https://doi.org/10.1175/1520-0469(1996)053<3236:WPOLAI>2.0.CO;2.

——, 2004: The shape of continents, air–sea interaction, and the rising branch of the Hadley circulation. *The Hadley Circulation: Past, Present and Future*, H. F. Diaz and R. S. Bradley, Eds., Kluwer Academic, 121–152.

——, and S. G. H. Philander, 1994: A coupled ocean–atmosphere model of relevance to the ITCZ in the eastern Pacific. *Tellus*, **46A**, 340–350, https://doi.org/10.3402/tellusa.v46i4.15484.

——, Q. Peng, Y. Kamae, X.-T. Zheng, H. Tokinaga, and D. Wang, 2018: Eastern Pacific ITCZ dipole and ENSO diversity. *J. Climate*, **31**, 4449–4462, https://doi.org/10.1175/JCLI-D-17-0905.1.

Zhang, C., 2001: Double ITCZs. *J. Geophys. Res.*, **106**, 11 785–11 792, https://doi.org/10.1029/2001JD900046.

——, 2005: Madden-Julian oscillation. *Rev. Geophys.*, **43**, RG2003, https://doi.org/10.1029/2004RG000158.

Zhang, G. J., and N. A. McFarlane, 1995: Sensitivity of climate simulations to the parameterization of cumulus convection in the Canadian Climate Centre general circulation model. *Atmos.–Ocean*, **33**, 407–446, https://doi.org/10.1080/07055900.1995.9649539.

Zhang, H., A. Clement, and P. Di Nezio, 2013: The South Pacific meridional mode: A mechanism for ENSO-like variability. *J. Climate*, **27**, 769–783, https://doi.org/10.1175/JCLI-D-13-00082.1.

——, C. Deser, A. Clement, and R. Tomas, 2014: Equatorial signatures of the Pacific meridional modes: Dependence on mean climate state. *Geophys. Res. Lett.*, **41**, 568–574, https://doi.org/10.1002/2013GL058842.

——, A. Clement, and B. Medeiros, 2015: The meridional mode in an idealized aquaplanet model: Dependence on the mean state. *J. Climate*, **29**, 2889–2905, https://doi.org/10.1175/JCLI-D-15-0399.1.

Zhou, W., and S.-P. Xie, 2017: Intermodel spread of the double-ITCZ bias in coupled GCMs tied to land surface temperature in AMIP GCMs. *Geophys. Res. Lett.*, **44**, 7975–7984, https://doi.org/10.1002/2017GL074377.

Unauthenticated | Downloaded 12/07/22 10:48 PM UTC